**Titre:** Influence of the Discontinuities on the Fatigue Behavior of Welded 410NiMo Turbines
Title:

**Auteur:** Forough Akbarian
Author:

**Date:** 2024

**Type:** Mémoire ou thèse / Dissertation or Thesis

**Référence:** Akbarian, F. (2024). Influence of the Discontinuities on the Fatigue Behavior of Welded 410NiMo Turbines [Mémoire de maîtrise, Polytechnique Montréal]. PolyPublie. https://publications.polymtl.ca/57724/
Citation:



**URL de PolyPublie:** https://publications.polymtl.ca/57724/
PolyPublie URL:

**Directeurs de recherche:** Myriam Brochu, & Pierre-Antony Deschênes
Advisors:

**Programme:** Génie mécanique
Program:

**POLYTECHNIQUE MONTRÉAL**

affiliée à l'Université de Montréal

# Influence of the Discontinuities on the Fatigue Behavior of Welded 410NiMo Turbines

**FOROUGH AKBARIAN**

Département de génie mécanique

Mémoire présenté en vue de l'obtention du diplôme de *Maîtrise ès sciences appliquées*
Génie mécanique

Février 2024

**POLYTECHNIQUE MONTRÉAL**

affiliée à l'Université de Montréal

Ce mémoire intitulé :

Influence of the Discontinuities on the Fatigue Behavior of Welded 410NiMo Turbines

présenté par **Forough AKBARIAN**

en vue de l'obtention du diplôme de *Maîtrise ès sciences appliquées*

a été dûment accepté par le jury d'examen constitué de :

**Aurelian VADEAN**, président

**Myriam BROCHU**, membre et directrice de recherche

**Pierre-Antony DESCHÊNES**, membre et codirecteur de recherche

**Vincent DEMERS**, membre

# DEDICATION

*To my loving husband, Sobhan, and my parents, Kimia and Sadegh, for their boundless support, encouragement, and love throughout this challenging journey.*

# ACKNOWLEDGEMENTS

The Institut de recherche d'Hydro-Québec (IREQ), SACMI, the natural sciences and Engineering Research council of Canada (NSERC), and the Consortium de recherche et d'innovation en transformation métallique (CRITM) provided the financial backing of this project. We would also like to express our gratitude for the valuable contributions and collaborations of Manon Provencher and C. Baillargeon, R. Dubois and Alexandre Bois Brochu (from CMQ).

# RÉSUMÉ

La durée de vie en fatigue des turbines hydroélectriques est principalement limitée par la défaillance en fatigue des pièces soudées en raison de la présence de discontinuités. Ainsi, il est essentiel de comprendre l'influence des discontinuités sur la résistance à la fatigue des matériaux afin de planifier l'inspection, la maintenance et la prédiction de la durée de vie en fatigue. Sur la base des investigations expérimentales et théoriques, divers outils de conception ont été développés pour prédire la résistance à la fatigue et la durée de vie du matériau soudé 410NiMo largement utilisé dans la fabrication de turbines hydroélectriques. Cependant, les outils de conception disponibles, tels que le diagramme Kitagawa-Takahashi (K-T), ne sont pas en mesure de prédire avec précision la résistance à la fatigue et la durée de vie. Leur précision et fiabilité sont remises en question. En 2019, un partenariat international en collaboration avec Hydro-Québec, appelé Projet de Recherche International sur la Fatigue-Corrosion (FatCo), a été lancé dans le but principal d'étudier le comportement de la corrosion et de la fatigue de l'alliage 13%Cr-4%Ni dans les turbines hydroélectriques. Dans le contexte du projet FatCo, l’objectif de cette recherche est d’analyser l’impact des discontinuités sur la résistance à la fatigue du matériau soudé 410NiMo.

Dans ce projet, deux parties d'analyse par éléments finis et d'essais de fatigue expérimentaux sont présentés. Les caractéristiques des discontinuités telles que le facteur de concentration de contrainte ($k_t$), l'exposant de singularité ($\alpha$) et la taille de la zone de contrainte maximale ont été déterminées par l'analyse par éléments finis (AEF). Un plan expérimental faisant intervenir des discontinuities artifielles a été élaboré à partir de l'examen de la littérature et des resultats par AEF. Des entailles hémisphériques d'une profondeur de 0.2, 0.5, 1 et 2 mm, toutes avec la même acuité ($\zeta$) de 1, ont été fabriquées sur des échantillons de fatigue. Les essais de fatigue ont été effectués selon la méthode par paliers à $R$ = 0.1 et $N = 2\times10^6$ cycles. Les résultats expérimentaux et de l'AEF ont été utilisés pour proposer un diagramme K-T modifié. Ce dernier a été comparé aux résultats analytiques d'autres théories d'entaille, telle que la théorie de la distance critique (TCD).

Les résultats révèlent que la résistance à la fatigue des entailles ne suit pas la tendance estimée par la mécanique linéaire élastique de la rupture (MLER) presentée dans un diagramme K-T. Les différences entre la moyenne de la résistance à la fatigue des expériences et la prédiction MLER augmentent avec l'augmentation de la taille des entailles de 0.2 à 2 mm. Un diagramme K-T modifié connu sous le nom de diagramme Atzori-Lazzarin (A-L) a fourni une prédiction

précise des données expérimentales. Étant donné que le champ de contrainte autour des entailles hémisphériques était différent de celui des fissures, l'exposant de singularité des entailles ($\alpha$ = 0.18) était inférieur à 0.5, ce qui concorde avec les valeurs prédites par la simulation par AEF. Selon les résultats, les points de transition de comportement en fatigue ($a_{0,n}$ et $a_n$*) ainsi que $\Delta K_{th}$ pour les entailles hémisphériques étaient égaux à 0.1 mm, 4.7 mm et 178 MPa.m$^{0.18}$, respectivement. Ces valeurs différaient de celles prédites pour les entailles de type fissure. De plus, l'étude a montré que lorsque les tailles des entailles (0.2 mm) se situent dans la plage de taille des discontuités, les fissures de fatigue peuvent s'amorcer à partir des discontinuités naturelles du matériau, et il y a une compétition entre l'entaille et les discontinuités de soudage pour des tailles de l'ordre 300 µm et moins.

# ABSTRACT

The lifespan of hydroelectric turbine runners is mainly limited by the fatigue failure of welded parts due to the presence of discontinuities. Therefore, understanding the influence of discontinuities on the fatigue strength of material is necessary to plan the inspection, maintenance and prediction of lifespan. Based on the experimental and theoretical investigations, several design tools have been modified to assess the fatigue strength and lifespan of 410NiMo welded material which is widely used in the fabrication of hydroelectric turbines. However, the available design tools, such as Kitagawa-Takahashi diagram (K-T), unable to predict the fatigue strength and lifespan precisely. Therefore, their precision and reliability are being questioned. In 2019, an international partnership in collaboration with Hydro-Quebec referred to as the Fatigue-Corrosion International Research Project (FatCo) was launched with the primary aim of investigation of the corrosion and fatigue behavior of 13%Cr-4%Ni alloy in hydroelectric turbines. As part of the FatCo project, this research work is defined to determine the influence of discontinuities on the fatigue strength of the welded 410NiMo material.

In this project, two parts of finite element analysis (FEA) and experimental fatigue tests are considered. The characteristics of discontinuities such as stress concentration factor ($k_t$) and singularity exponent ($\alpha$) were determined by the FEA. An experimental plan involving artificial discontinuities was thought out on the basis of the literature review and the results in FEA. Hemispherical notches with depths of 0.2, 0.5, 1 and 2 mm all with the same acuity ($\zeta$) of unity, were manufactured on fatigue specimens. The fatigue tests are conducted according to step method at $R$= 0.1 and $N$= $2\times10^6$ cycles. The experimental and FEA results were used to propose a modified K-T diagram. The latter was compared to analytical results from other notch theories, such as theory of critical distance (TCD).

The results reveal that the fatigue strength of notches does not follow the trend estimated by the linear elastic fracture mechanics (LEFM) presented in the K-T diagram. The differences between the average of fatigue strength of experiments and LEFM prediction increases with increasing notch sizes from 0.2 to 2 mm. A modified K-T diagram known as Atzori-Lazzarin (A-L) diagram provided a precise prediction with the experimental data. Since the stress field around hemispherical notches was different from cracks, the singularity exponent of notches ($\alpha$= 0.18) was smaller than 0.5 which is in good agreement with the predicted values by the FEA. Based on the findings, the transitions points of the fatigue behavior ($a_{0,n}$ and $a_n$*) as well

as $\Delta K_{th,n}$ for hemispherical notches were equal to 0.1 mm, 4.7 mm and 178 $MPa.m^{0.18}$, respectively. These values differed from those predicted for crack-like notches. Additionally, the study showed that when the notch sizes (0.2 mm) are in the range of natural discontinuities, fatigue cracks could initiate from material's natural discontinuities and there is a competition between notch and weld discontinuities in the size range of 300 µm or less.

# TABLE OF CONTENTS

# LIST OF TABLES

# LIST OF FIGURES

# LIST OF SYMBOLS AND ABBREVIATIONS

| | |
|---|---|
| $\alpha$ | Singularity exponent |
| $\Delta K$ | Stress intensity factor range |
| $\Delta K_{th}$ | Threshold stress intensity factor range |
| $\Delta K_{th,n}$ | Threshold stress intensity factor range for notches |
| $\Delta\sigma$ | Stress range |
| $\Delta\sigma_0$ | Fatigue limit of smooth and defect less specimen |
| $\zeta$ | Acuity of the notch |
| $\upsilon$ | Poisson ratio |
| $\rho$ | Notch tip radius |
| $\sigma_a$ | Nominal stress amplitude |
| $\sigma_d$ | Local stress at distance *d* from the notch |
| $\sigma_{local}$ | Local stress |
| $\sigma_{nominal}$ | Nominal stress |
| $\sigma_{UTS}$ | Ultimate tensile strength |
| $\sigma_Y$ | Yield strength |
| $\sigma_{yy}$ | Maximum local stress in Y direction |
| $\phi$ | Diameter of test specimen |
| $a$ | Crack length or discontinuity size |
| $a_0$ | Transition point in K-T diagram from short to long cracks |
| $a_{0,n}$ | Transition point in A-L diagram |
| $a^*$ | Transition point from long crack to notch approach in K-T diagram |
| $a_n^*$ | Transition point in A-L diagram from stress field to peak stress zone |
| *AM* | Area method |

| | |
|---|---|
| *A-L* | Atzori-Lazzarin |
| $c_p$, $c_N$ | Material constants |
| *CNP* | Centered notch plate |
| *DENP* | Double edge notch plate |
| $e_f$ | Elongation to fracture |
| *EDS* | Energy dispersive spectroscopy |
| *FCAW* | Fluxed core arc welding |
| *FEA* | Finite element analysis |
| *GDS* | Glow discharge spectroscopy |
| *K-T* | Kitagawa-Takahashi |
| $k_t$ | Stress concentration factor |
| $k_f$ | Fatigue notch factor |
| *LEFM* | Linear elastic fracture mechanics |
| *LM* | Line method |
| $N$ | Number of fatigue cycles |
| $n$ | Number of steps |
| $N_f$ | Number of fatigue cycles at failure at specific step |
| *NNE* | No notch effect |
| *NSF* | Notch stress field |
| *OM* | Optical microscope |
| *PWHT* | Post weld heat treatment |
| $R$ | Cyclic stress ratio |
| *SEM* | Scanning electron microcope |
| *TCD* | Theory of critical distance |
| *VM* | Volume method |

| | |
|---|---|
| *X* | Distance from root of the notch |
| *XRD* | X-ray diffraction |
| *Y* | Geometry factor |

# LIST OF APPENDICES

# CHAPTER 1 INTRODUCTION

Francis turbine runners are components of turbine systems that convert kinetic energy of flowing water into electrical energy. It allows for adjustments of the flow rates and water direction in the turbine. Figure 1-1 shows a typical Francis turbine runner consisting of several blades welded to a top and bottom part called the crown and band, respectively.

One of the in-service challenges of turbine runners is fatigue failure [1]. Fatigue damage reduces the lifespan of the turbine runners and increases downtimes in production. One approach to limit the risk of fatigue failure is inspection and maintenance. Fatigue life prediction supports planning these activities. In the year 2019, an international partnership in collaboration with Hydro-Quebec referred to as the Fatigue-Corrosion International Research Project (FatCo) was formed with the primary aim of investigating of the corrosion and fatigue behavior of hydroelectric turbines.

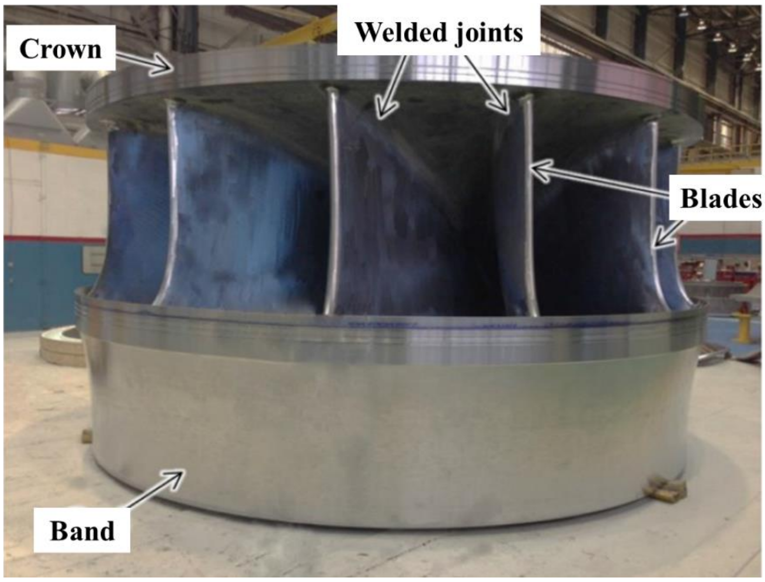


Figure 1-1 Francis hydroelectric turbine runner consisting of blades welded to the crown and the band [2].

Hydroelectric turbine runners are manufactured from martensitic stainless steels like the 13%Cr-4%Ni materials. These family of steels are a preferred choice due to their combination of high strength, good toughness [3] and good weldability [4]. For both repairing and manufacturing purposes, it is common to use multipass welding on the 13%Cr- 4%Ni steel. The optimal selection of filler material in such cases is typically ER410NiMo, having a similar chemical composition to that of the base material.

Numerous studies indicate that the welded 410NiMo steel has a martensitic microstructure with different discontinuities, such as non-metallic inclusions, pores, and lack of fusions [5, 6]. These discontinuities may act as stress raisers that could lead to crack initiation and propagation, ultimately affecting the fatigue strength of the runner. Cracks emanating from certain sharp discontinuities may have insignificant initiation life because the stress concentration is high enough to initiate a crack, while others, emanating from blunt notches may initiate after numerous load cycles [7].

Researchers find challenging the evaluation of the behavior of cracks emanating from discontinuities. For instance, Gagnon et al. [8, 9], assumed that the casting defects in CA6NM material are sharp and the time required for crack initiation is very short. Based on this concept using linear elastic fracture mechanics (LEFM), a Kitagawa-Takahashi (K-T) diagram solely based on the crack propagation kinetic [10] is used by Hydro-Quebec to design the hydroelectric turbines. The K-T diagram has been applied as a tool in predicting the operational life of turbines for a long time. Nevertheless, the industry's empirical experience in several cases showed that the actual lifespan of hydroelectric turbines exceeded the predictions. These instances questioned the precision and accuracy of such predictions. This is because LEFM approach has limitations dealing with discontinuities characterized by stress field which are not comparable to those of ahead of sharp cracks.

Several researchers attempted to provide a more accurate prediction of fatigue strength and lifespan of structures by linking the LEFM and notch approaches. The theory of critical distance (TCD) by Taylor [11], an adaptation of the pioneering contributions by Peterson [12] and Neuber [13], proposed a model to understand the behavior of cracks and notches by using a unified approach. In the TCD model, the analysis takes into account the elastic stress within a critical distance ahead of the discontinuity. Atzori and Lazzarin [14] proposed a generalized K-T diagram to explain the crack and notch behavior using the notch stress intensity factor rather than the classical stress intensity factor of the LEFM approach. This diagram is considered as an improved and extended K-T diagram.

Each of the mentioned approaches has their specific limitations and it is necessary to establish which one is more accurate for the specific application of crack emanating from welding discontinuities. Hence, this research work hopes to answer the following question: "Could the use of notch approaches improve the fatigue strength prediction of welded turbines?". This thesis gives an outline of the project's literature review, materials and methods, results, and an analysis that interprets those results.

Chapter 2 contains a literature review with three main sections. The first section outlines the typical characteristics of welded 410NiMo material. The second section provides an overview of the impact of crack-like discontinuities on the fatigue strength, while the third section explains the concept of notch theories. The project's specific objectives are proposed based on the available literature. Chapter 3 outlines the project’s methodology. It begins by introducing the test plan and then, the materials properties and test methods are discussed. In chapter 4, the results regarding the effect of notch on the fatigue strength of welded material with specific discussion will be presented. While the discussion on the results is provided in chapter 4, the chapter 5 includes the conclusion, limitations of this project and recommendations for the future researches.

# CHAPTER 2 LITERATURE REVIEW

The first subsection of this chapter will cover the characteristics of 13%Cr-4%Ni alloy. The subsequent part will review the Kitagawa-Takahashi diagram and notch theories. The final section will establish the project objectives, aimed at filling gaps in current knowledge.

## 2.1 Nominal characteristics of the welded 410NiMo

### 2.1.1 Welded 13%Cr-4%Ni material

Martensitic stainless steels are used for manufacturing hydraulic turbine runners and gas turbines. Among different alloys in the family of martensitic steels, the low carbon 13%Cr-4%Ni steel is available in cast and wrought forms known as CA6NM and AISI 415 stainless steel, respectively. Welding is frequently used in the production and maintenance of turbines and is often regarded as a rapid solidification process. Various components of turbine runners, such as blades and crown, are joined together by welding. Hydroelectric runners are typically manufactured using the fluxed cored arc welding (FCAW) due to its ability to achieve a high deposition rate [15]. It is a welding process that utilizes a continuously fed wire electrode that is filled with flux. This wire electrode is passed through a welding gun creating an electric arc between the wire and the base material. This arc generates heat to melt the wire and the base material. The flux contained in the wire electrode melts and creates a shielding gas to avoid the contact of the molten weld pool and atmosphere. During the FCAW process, mixture of $CO_2$ and argon is used to protect the welding pool to provide higher welding rate and arc stability. The quality of the weld can significantly impact the performance and reliability of the turbine runner. Several factors affect the quality of a weld, such as the selection of the filler material. To limit the stress raising by discontinuities, it is preferable that the filler material have physical and mechanical properties comparable to the base metal.

In order to reduce the mismatch between the chemical composition of base and the weld metal, a fluxed-core filler material called ER410NiMo is used to weld the 13%Cr-4%Ni base material in the Francis turbine runners. The choice of ER410NiMo filler material is based on several factors, such as the material's properties and the weldability. As reported in Table 2- 1, ER410NiMo has a chemical composition similar to the base material. Adding chromium to the composition of these alloys improves the development of martensite and corrosion resistance while low carbon content reduces the hot cracking susceptibility.

Table 2- 1 Nominal chemical composition of AISI 415 [3] and ER410NiMo [16].

| **Wt.% elements*** | **C** | **Mn** | **P** | **S** | **Si** | **Cr** | **Ni** | **Mo** |
|---|---|---|---|---|---|---|---|---|
| **AISI 415** | 0.05 | 0.5-1.0 | 0.030 | 0.030 | 0.60 | 11.5-14.0 | 3.5-5.5 | 0.5-1.0 |
| **ER410NiMo** | 0.06 | 1.0 | 0.04 | 0.03 | 0.5 | 11.0-12.5 | 4.0-5.0 | 1.0 |

* single values are the maximum allowed content.

### 2.1.2 Microstructure characterization

The microstructure of a weld is influenced by its chemistry and heat cycles it is subjected to. In the case of multipass welding, each pass generates heat that affecting the microstructure of previous pass. To reduce the effects of multi-pass welding, post-weld heat treatment (PWHT) is required. PWHT is a controlled heating and cooling process performed on welded structures when the welding process finishes. It lowers the hardness and relaxes the residual stresses in the martensitic microstructure [17]. Foroozmehr et al.[18] investigated the microstructure of a 410NiMo multipass weld heat treated at 600˚C for 1 hour. Their result using optical microscope (OM), in Figure 2-1, shows that the microstructure is mainly composed of martensite laths.

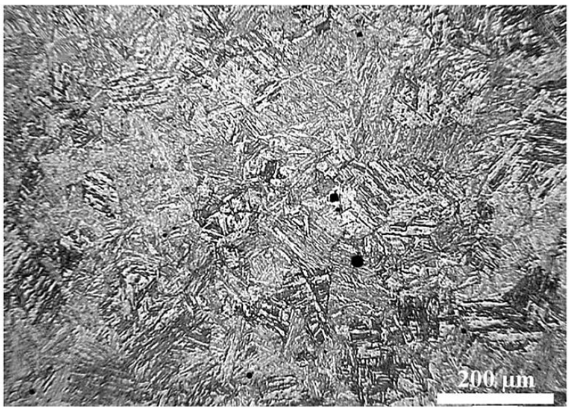


Figure 2-1 Microstructure of 410NiMo weld material after heat treatment at 600˚C and 2 hours [18].

Depending on the tempering temperature, austenite can also form during the PWHT process. This austenite is named reformed austenite to differentiate it from the residual austenite. As demonstrated in the work of Godin et al. [19] and Song et al. [20], the volume fraction of austenite is affected by factors including time and temperature. It ranges from 0 to 27% as reported in the work of Tenni et al. who used the X-ray diffraction method (XRD) to quantify the content of austenite in the welded 410NiMo material after PWHT [21].

### 2.1.3 Mechanical properties

Through heat treatment, optimized mechanical properties of the welded AISI 415 stainless steel is achieved. According to the ASTM A240 and ASTM A5 standards [3, 16], the minimum ultimate tensile strength of AISI 415 and 410NiMo weld are 795 and 760 MPa, respectively while both have at least a 15% elongation.

### 2.1.4 Welding discontinuities in 410NiMo

Similar to all liquid phase manufacturing processes such as casting and additive manufacturing, welding produces discontinuities. Since oxygen is always present in the environment, it could mix with elements of the weld pool and produce oxides. Also, there are various oxides of zirconium, silicon and titanium in the flux core of the FCAW electrode that may be entrapped in the weld pool [6]. Apart from the chemical composition, shape, size and geometry are other variables used to characterize discontinuities. Tenni et al. [22] observed oxide inclusions on the fracture surface of the 410NiMo welded material using scanning electron microscope (SEM). As shown in Figure 2-2, the oxide inclusions are rounded and mainly composed of manganese, zirconium, silicon and titanium using energy dispersive spectroscopy (EDS). It is reported that the average diameter of these oxide inclusions is between 1-5 µm.

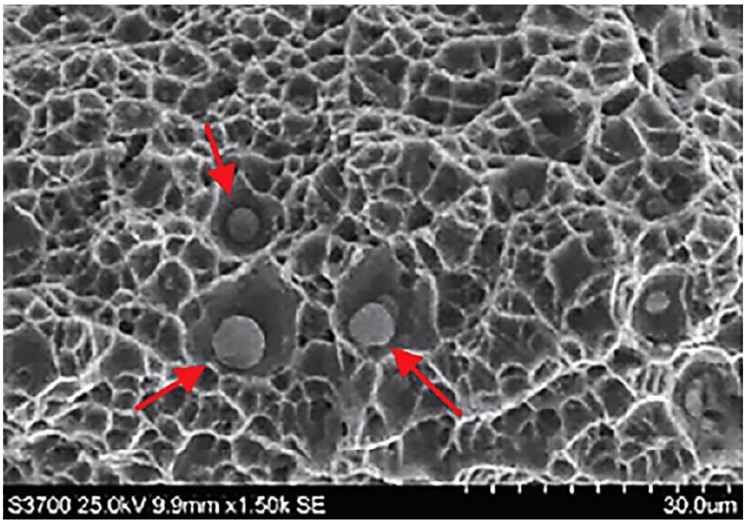


Figure 2-2 SEM observations of 410NiMo weld material (a) oxide inclusions (b) EDS results [22].

Voids and porosities are other types of discontinuities observed in the welded 410NiMo material. Boukani et al. [6] provided the results of metallographic characterization performed on a multipass 410NiMo welded material as shown in Figure 2-3. According to the author's observations, a semicylindrical void, filled with an inclusion between two passes after gouging (gouging refers to removal of unwanted weld material from a workpiece), is elongated through the thickness of the material like a wormhole. The diameter of this void is about 300 µm and it is almost 4 mm in length.

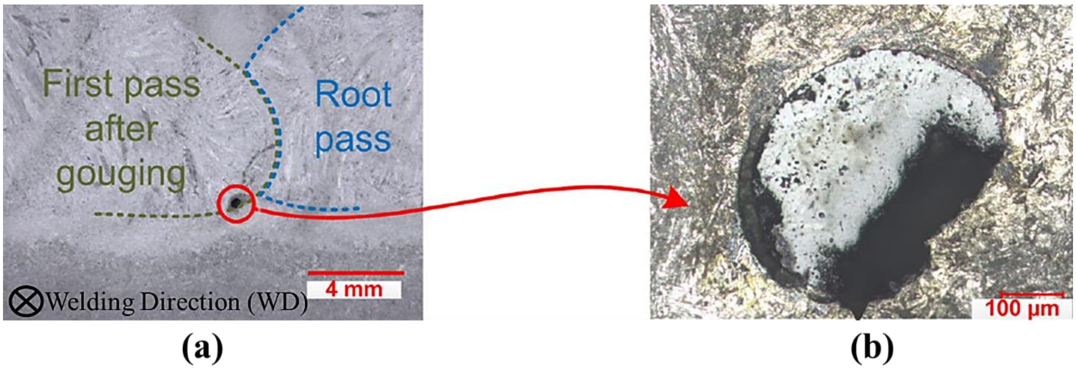


Figure 2-3 Microscopic observations of a discontinuity (a) between two passes and (b) higher magnification of discontinuity in (a) in the 410NiMo weld material [6].

Due to the rapid solidification and cooling in the welded zone, lack of fusion can be created upon shrinkage. Based on the metallographic observations performed at Hydro-Quebec research institute [23], as depicted in Figure 2-4, lack of fusions having a width of more than 500 µm elongated between weld beads are common discontinuities.

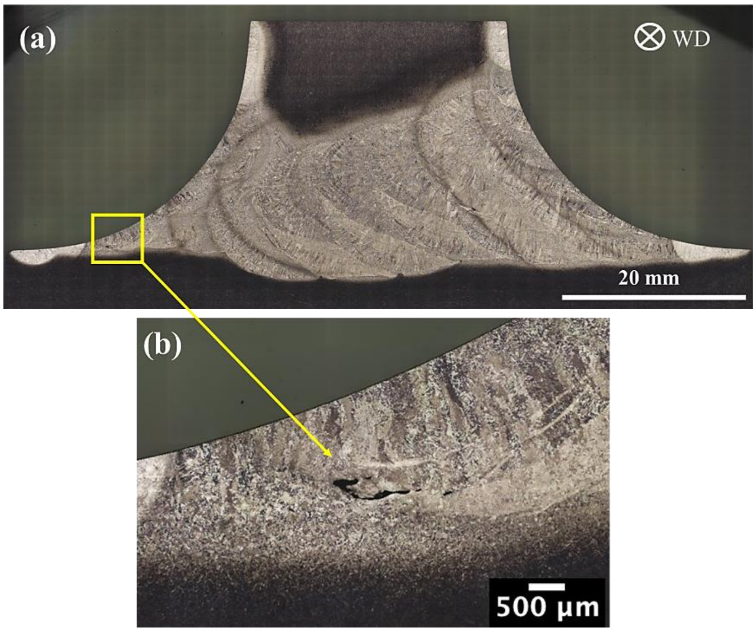


Figure 2-4 Macrographs of (a) a T-joint extracted weld sample and (b) the close view of a typical lack of fusion in 410NiMo welded material [23].

## 2.2 Influence of discontinuities on the fatigue strength

### 2.2.1 LEFM approach

Discontinuities present in a material can trigger fatigue crack initiation under cyclic stress. These cracks, once initiated, can propagate and cause failure under favorable conditions [24]. Generally, there is a relationship, whereby larger discontinuity tends to result in lower fatigue strength. As shown in Figure 2-5, for a cast aluminum alloy, the fatigue strength at $10^7$ cycles decreases proportional to the inclusion's size.

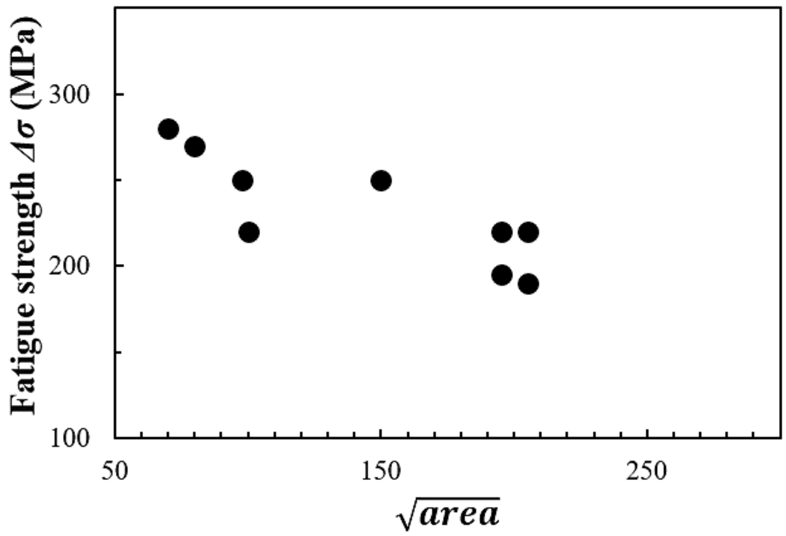


Figure 2-5 Fatigue strength for $10^7$ cycles as a function of inclusion size ($\sqrt{area}$) for a cast aluminum alloy tested at $R$= -1 [extracted data from [25]].

One of the widely used fatigue design tools in academics and industries is the Kitagawa-Takahashi diagram [26]. This diagram is a graphical representation of the relationship between the fatigue strength ($\Delta\sigma$) and the size of discontinuities. The K-T diagram is employed for a specific material with tested at a given stress ratio ($R$). As illustrated in Figure 2-6, the diagram combines the fatigue limit ($\Delta\sigma_0$) of flawless specimens, determined based on the ASTM E466 standard [27], and the threshold stress intensity factor range ($\Delta K_{th}$) of the material, obtained in accordance to the ASTM E647 [28], to define a safe zone where it is expected that there will be no failure.

The threshold line ($\Delta\sigma = \frac{\Delta K_{th}}{Y.\sqrt{\pi a}}$) is based on the linear elastic fracture mechanics (LEFM) approach. The LEFM quantifies the stress intensity of cracks affected by the cyclic stress ($\Delta\sigma$), crack size ($a$) and geometry factor ($Y$) under linear-elastic conditions [29] as per Equation (2-1).

$\Delta K = \Delta\sigma.\ Y\sqrt{\pi a}$ (2-1)

Experiments have shown that a crack will propagate only if $\Delta K \geq \Delta K_{th}$. Therefore, when LEFM applies, the fatigue strength can be expressed by the equation (2-2):

$\Delta\sigma = \frac{\Delta K_{th}}{Y.\sqrt{\pi a}}$ (2-2)

Under a certain size, characterize in the K-T diagram by $a_0$, the LEFM theory cannot be used to predict if a crack will or will not propagate. Based on this observation, the K-T diagram is divided in two regions of short and long cracks. Short cracks could have sizes of microsturctural features like the grain size or larger and have unpredictable propagation behavior. Thus, the response of short cracks to propagation is not dependent on the material $\Delta K_{th}$. For instance, they can propagate at $\Delta K$ lower than $\Delta K_{th}$ [30]. In contrast, long cracks exhibit a dependency on the material threshold as such their behavior is predictable. Therefore, the LEFM approach is widely adopted for analysis and life prediction of components containing long cracks.

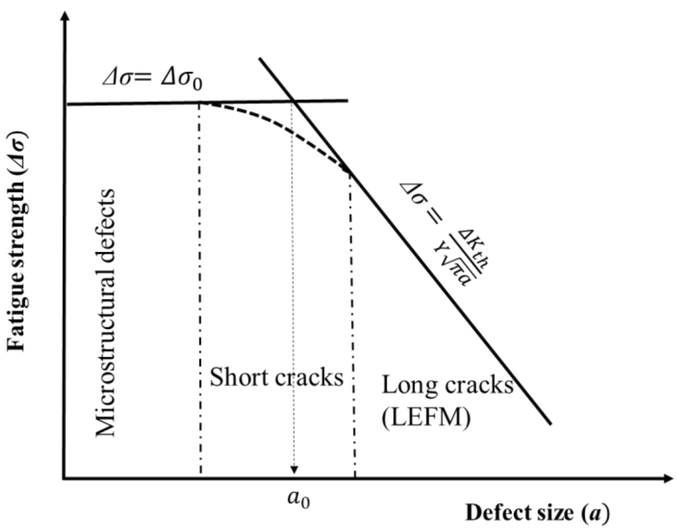


Figure 2-6 Schematic view of a Kitagawa-Takahashi diagram [modified from [26]].

From Figure 2-6, $a_0$ marks the transition point between a behavior that can be predicted by the LEFM and the value of $\Delta\sigma_0$. El-Haddad et al. [31] proposed that $a_0$ (named as $l_0$ in the original paper) can be used to predict the behavior of cracks diverging to the LEFM prediction. It is a material parameter that is related to the smallest microstructural feature [31]. Equation 2-3 shows the mathemtatical definition of $a_0$ based on the intersection of LEFM stress intensity threshold expression and the fatigue limit of flawless material.

$$a_0 = \frac{1}{\pi} \left(\frac{\Delta K_{th}}{Y.\Delta\sigma_0}\right)^2 \qquad (2\text{-}3)$$

The K-T diagram is useful for evaluating the fatigue strength of components containing cracks and small discontinuities based on LEFM. However it is limited in its application when the stress distribution ahead of the discontinuity is different from the stress field ahead of a crack. The next sections discuss the literature approaches accounting for discontinuties with different stress distributions.

## 2.2.2 Notch approaches

### 2.2.2.1 Definition of the notch parameters

***Stress concentration factor ($k_t$)***

A notch is any geometrical feature such as holes and fillets that locally raises the stress [29]. Metallurgical discontinuities such as inclusions and lack of fusions can also behave like notches. Figure 2-7 illustrates a schematic view of a notch with depth of "*a*" and tip radius of "*ρ*".

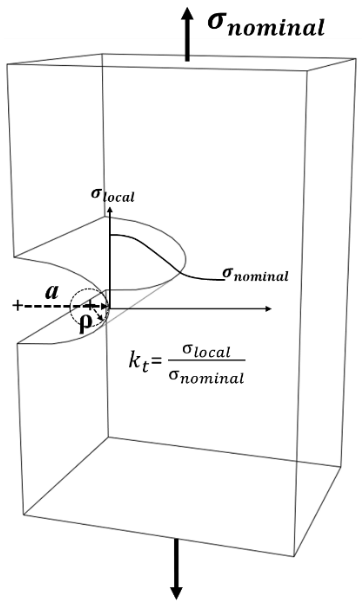


Figure 2-7 Schematic view of a through all notch with depth of *a* and tip radius of *ρ*.

The existance of a notch causes local stress concentration described by a factor '$k_t$' referred to as the stress concentration factor. The $k_t$ is thought of as a numerical value used to quantify the increase in applied stress at a notch location on a component [29]. It is a dimensionless factor that quantifies the ratio of the $\sigma_{local}$ (peak stress) at the root of the notch by the $\sigma_{nominal}$ applied to the material (see equation 2-4). The notch is different from the crack for which the stress concentration factor is infinite since the tip radius of a crack approaches zero.

$$k_t = \frac{\sigma_{local}}{\sigma_{nominal}} \quad (2\text{-}4)$$

For simple geomteries, the $k_t$ can be predicted analytically based on the notch dimensions as given in equation (2-5). This is an equation very specific for a through all notch having a semi-elliptical shape (see Figure 2-7).

$$k_t = 1 + 2\sqrt{\frac{a}{\rho}} = 1 + 2\sqrt{\zeta} \quad (2\text{-}5)$$

where the ratio of depth over radius is known as notch acuity ($\zeta$). Accordingly, the stress concentration factor changes proportional to the square root of the acuity. In other words, an increase in the "$a$" or a decrease in the "$\rho$" will result in a higher stress concentration factor. For most notches, $k_t$ can be quantified by the above mentioned equation or finite element analysis (FEA). For instance, Pessard et al. [32] determined the stress concentration factor around the notch tip for a blind hemispherical notch using Abaqus simulation. In this model, the Young's modulus of 110 GPa and poison ratio of $\upsilon$= 0.34 were used to characterize a titanium alloy. As given by Figure 2-8, a nominal stress of 1 MPa was applied on the block in Y-axis. Elastic simulation results converged toward a stress concentration factor equal to 2, as illustrated by the maximum value of the local stress (2.036 MPa).

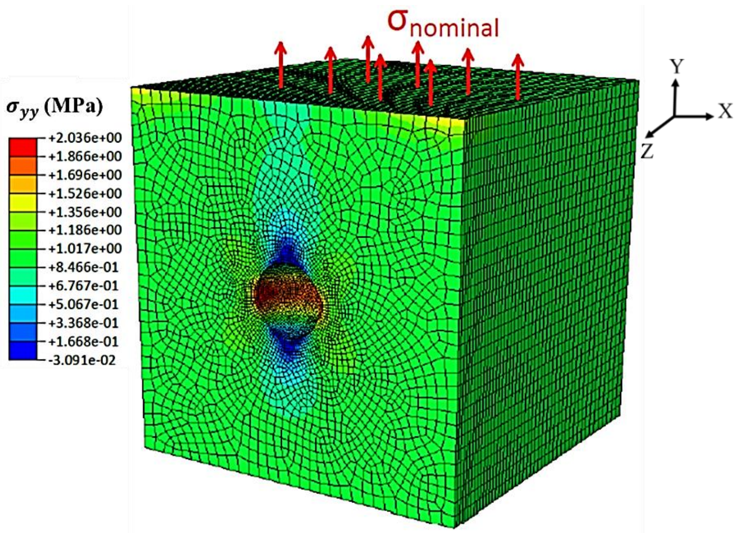


Figure 2-8 Determining the $k_t$ and $\sigma_{local}$ of a notch with depth and radius of 300 μm under axial nominal stress of 1 MPa by FEA [32].

The stress level around the notch is not constant, it decreases with an increasing distance from the notch. Figure 2-9 schematizes the stress evolution in the z direction. The stress field of the notch is bounded by the region where the the local over the nominal stress ($\frac{\sigma_{local}}{\sigma_{nominal}}$) reaches its maximum value, up to the point where this ratio equals one [33]. The slope of this graph (in log scale) gives the singularity exponent "$\alpha$" which is influenced by the notch dimensions.

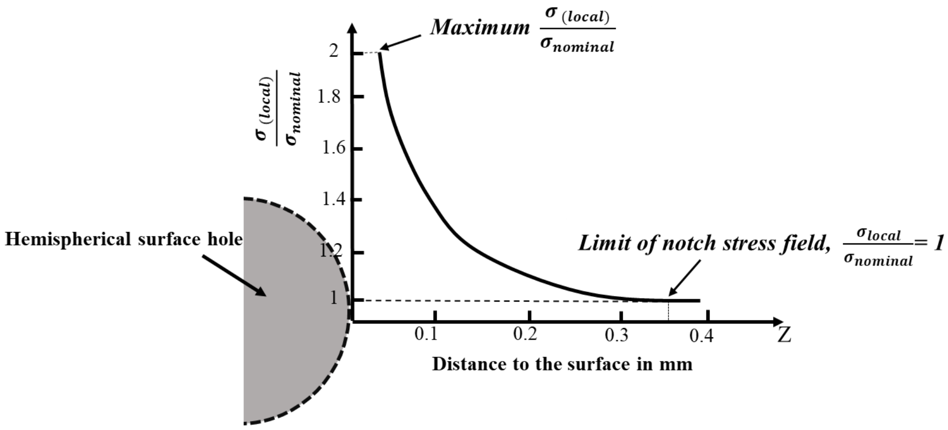


Figure 2-9 Stress distribution as a function of the distance from the notch tip [modified from [32]].

For instance, consider the case of a notch having the same $k_t$ (same $\zeta$) but of different sizes as shown in Figure 2-10a. Figure 2-10b shows that although the three notches possess the same $k_t$ and slope due to their constant acuity, their stress field limit extends with the notch dimensions [33]. One can imagine that a crack that initiates from notch 3, would propagate through a larger notch stress field in comparison to notch 2 and 1.

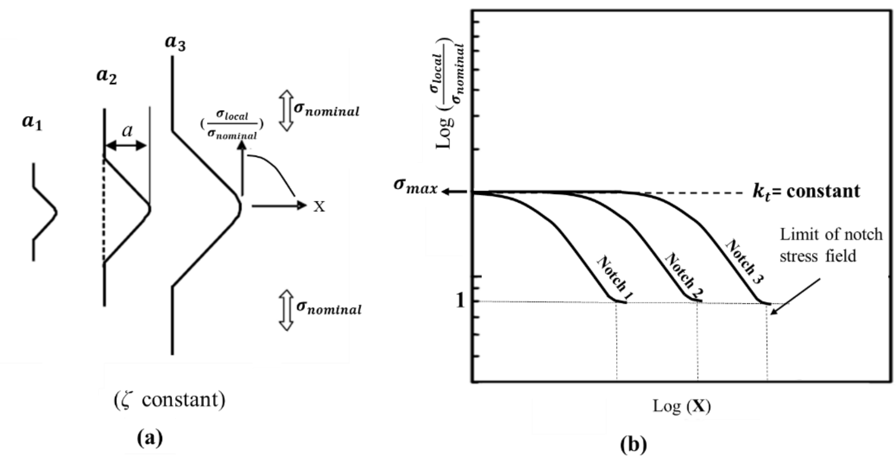


Figure 2-10 Stress distribution around notches with the same acuity and different sizes [modified from [33]].

Although $k_t$ plays an important role in determining the impact of notches on stress distribution and fatigue strength, additional factors need to be taken into account to predict their effect on a material resistance to fatigue.

***Fatigue notch factor ($k_f$)***

In the presence of a notch, one could expect that the material resistance to fatigue is reduced by a factor of $k_t$. However, it has been observed that in certain instances the notch's impact is less severe than $k_t$ [29]. Therefore, another factor known as the fatigue notch factor "$k_f$" was introduced to explain the effect of stress concentrators in fatigue. The $k_f$ is the ratio of fatigue resistance of smooth specimen ($\sigma_0$) to the fatigue strength of notched specimen ($\sigma_a$), as expressed in equation (2-6).

$$k_f = \frac{\sigma_0}{\sigma_a} \qquad (2\text{-}6)$$

For instance, Figure 2-11 illustrates that the experimental fatigue strength of notched martensitic material (triangle points) is above the $k_t$ estimation (dashed line). There are different physical reasons for the difference between $k_f$ and $k_t$. One argument based on the stress gradient explains that for crack initiation around the notch, the average stress over the stress field of the notch, instead of the peak stress, should be higher than the fatigue limit of material as will be explained in section 2.2.2.2 [29].

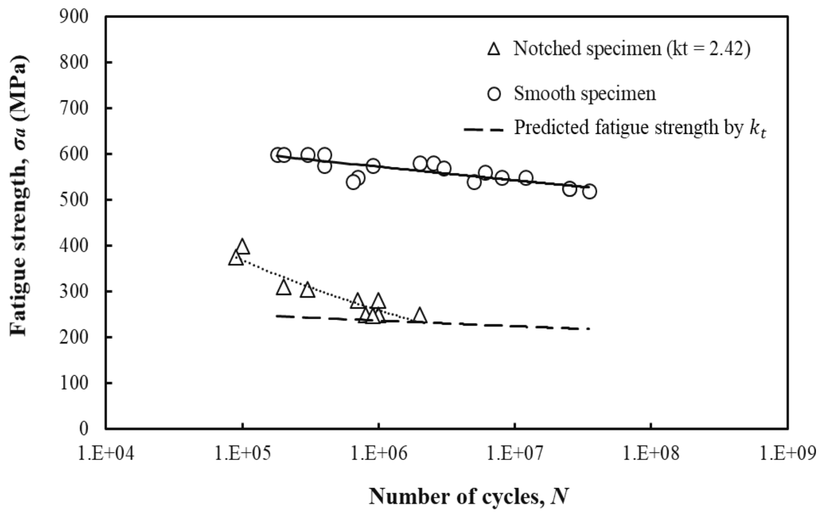


Figure 2-11 Effect of notches on the fatigue strength considering the effect of $k_t$ and $k_f$ (extracted from [34, 35]).

**2.2.2.2 Theory of the critical distance (TCD)**

The classical notch theories applied the concept of average stress, instead of peak stress, to determine the notch effect on the fatigue strength. For instance, Peterson [12] assumed that if the average stress at specific distance from the root of the notch is higher than the $\Delta\sigma_0$, fatigue damage occurs. Then, he derived the following empirical equation based on $k_f$ and $k_t$:

$$k_f = 1 + \frac{k_t - 1}{1 + \frac{c_p}{\rho}} \quad \text{(Peterson)} \tag{2-7}$$

Nueber [13] used the average stress over a specific distance ahead of the notch tip for estimation of the fatigue strength of notched specimen, as below:

$$k_f = 1 + \frac{k_t - 1}{1 + \sqrt{\frac{c_N}{\rho}}} \quad \text{(Neuber)} \tag{2-8}$$

In these equations, $c_p$ and $c_N$ are material constants and they are dependent on the $\sigma_{UTS}$ of the material. For a martensitic steel with the ultimate tensile strength in the range of 825-850 MPa, $c_p$ and $c_N$ are in the ranges of (125-150 µm) and (55-65 µm), respectively [36].

One of the main criticisms directed towards the classical $k_f$ formulas is that they only rely on the ultimate tensile strength while the fracture mechanic constants are ignored. Therefore, Taylor [11] extended the Nueber's and Peterson's theories and provided a general formulation known as theory of critical distance (TCD). In the presence of crack-like notch, critical distance was defined using the $a_0$ which is a material property dependent on $\Delta K_{th}$ and $\Delta\sigma_0$ (see equation 2-2). Consequently, he proposed different formulation to find the average stress that the most popular ones are point method (PM) and line method (LM). Figure 2-12 is a schematic view of the stress field at the tip of a notch where the critical distance for the point and line method are reported. In the PM, it is assumed that when the maximum stress perpendicular to the crack tip $\Delta\sigma$ at point $(x = \frac{a_0}{2})$ reaches the $\Delta\sigma_0$, fatigue damage will occur. The condition for crack initiation and propagation is as follows:

$$\Delta\sigma \left(x = \frac{a_0}{2}\right) \geq \Delta\sigma_0 \tag{2-9}$$

In the LM, the average of $\Delta\sigma$ at the notch bisector through a distance of ($x = 2a_0$) far from the peak stress ($x$=0) is determined by integrating as follows:

$$\frac{1}{2a_0} \int_0^{2a_0} \Delta\sigma(x)\, dx \tag{2-10}$$

When the result of this integration is larger than $\Delta\sigma_0$, fatigue damage occurs. It worths to mention that the TCD has other methodologies such as area method (AM) and volume method (VM) but they are not explained here for the aim of simplicity.

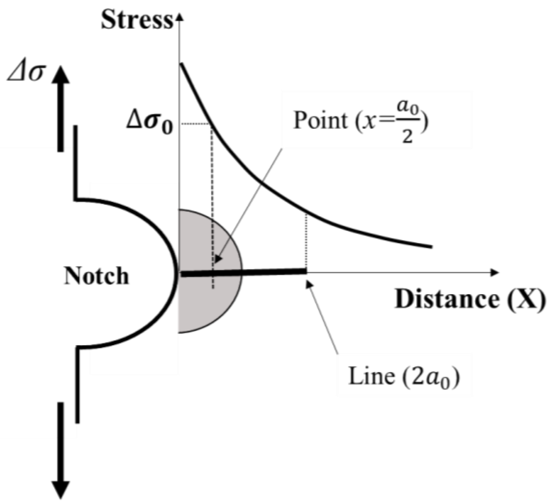


Figure 2-12 Schematic presentation of point and line method at the tip of a notch [modified from [11]].

Liu et al. [37] validated the experimental fatigue strength of different materials taken from literature with central (CNP) or double edge (DENP) notches using PM and LM, as illustrated in Figure 2-13. The material properties, test conditions and authors of the experiments are provided in Table 2-2. According to Table 2-3 and Figure 2-13, the accuracy of the PM is 60% while the accuracy of the LM is 77.7%. However, the PM gives more conservative results than the LM method.

Table 2-2 Material properties of selected materials.

| | Notch type | R | $\Delta\sigma_0$ (MPa) | $\Delta K_{th}$(MPa.$\sqrt{m}$) |
|---|---|---|---|---|
| ■ Mild steel [38] | DENP | -1 | 431 | 12.8 |
| ● SAE 4130 [39] | DENP | -1 | 648 | 8.5 |
| ▲ HT60 [40] | DENP | 0 | 580 | 13.0 |
| ▼ SAE 4130 [39] | CNP | -1 | 648 | 8.5 |
| ◆ SAE 1045 [41] | CNP | 0 | 448 | 6.9 |
| ◀ SAE 1045 [41] | CNP | -1 | 606 | 9.0 |
| ▶ 2024- T351 [41] | CNP | 0 | 172 | 4.0 |
| ⬣ 2024- T351 [41] | CNP | -1 | 248 | 4.4 |
| ★ G 40.11 [41] | CNP | -1 | 540 | 11.5 |

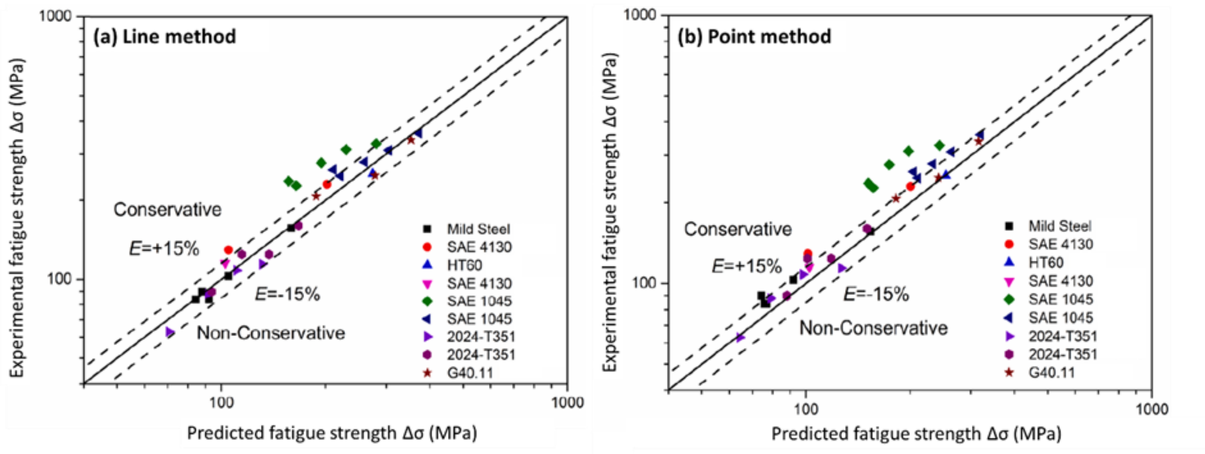


Figure 2- 13 Comparison of the fatigue strength of different materials with (a) Line method and (b) Point method [35].

Table 2- 3 Summary of the prediction results using LM and PM.

| Method | $-15\% \leq E \leq +15\%$ | $0 \leq E$ | $-15\% \leq E$ |
|---|---|---|---|
| Line method | 77.7% | 90.0% | 100% |
| Point method | 60.0% | 50.0% | 100% |

The main purpose of using abovementioned theories was predicting the fatigue strength of components in the presence of the notch focusing on identifying the critical stress that causes fatigue damage. However, it is well established that a stress gradient beyond the critical distances ($\frac{a_0}{2}$ or $2a_0$) also contributes to the notch effect on fatigue strength [33]. In the next section, Atzori and Lazzarin [42] explored this notch stress field concept using the notch stress intensity factor to propose a general model for notches with different dimensions and stress fields.

### 2.2.2.3 Theory of the notch stress intensity factor (NSIF)

The efforts of Atzori and Lazzarin to account for the effect of the notch stress field in the K-T diagram led to the observation of a deviating trend from the long crack approach. Thus, they proposed a modified K-T diagram shown in Figure 2-14, and it is now commonly referred to as the Atzori-Lazzarin diagram (A-L). The A-L diagram serves as an analytical tool that accounts for the effect of short cracks ($a < a_0$), long cracks ($a_0 < a < a^*$) and notches ($a > a^*$) on fatigue strength for a given $k_t$ and $\alpha$. In other words, this diagram gives a schematic view of the behavior notches having the same acuity.

Zone A and B in Figure 2-14 represents the original K-T diagram and the modified portion by Atzori and Lazzarin, respectively. A transition is observed between both zones signifying the trend from long crack to notch-like discontinuities. A characteristic size of discontinuity represented by $a*$ is adopted to identify the mathematical description of this transition region.

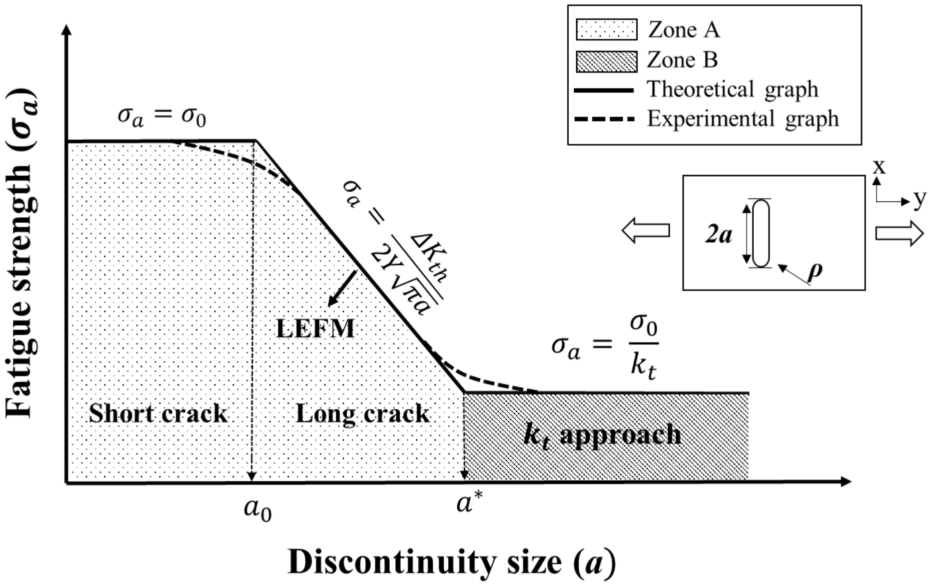


Figure 2-14 Schematic view of an Atzori-Lazzarin diagram for notches with $\alpha$= 0.5 [modified from [14]].

Figure 2-14 represents the cases of cracks and notches with a given $k_t$ having the same stress gradient characterized by $\alpha$ = 0.5 [14]. For $a > a*$, the lower horizontal line presents the nominal fatigue strength in the presence of blunt notch assuming that $k_t = k_f$ is:

$$\Delta\sigma = \frac{\Delta\sigma_0}{k_t} \tag{2-11}$$

The intersection of those lines lead to a unique value of "$a$" defined as "$a*$" expressed by equation (2-12), when combining equation (2-2) and (2-11):

$$a* = \frac{1}{\pi}\ (\frac{k_t\ .\ \Delta K_{th}}{Y\Delta\sigma_0})^2 \tag{2-12}$$

The critical crack length $a*$ is not only dependant on material properties ($\Delta K_{th}, \Delta\sigma_0$) but also on the notch geometries. Combining equation (2-12) and (2-3), a relation between $a*$ and $a_0$ is expressed as in equation (2-13) [14]. It worth to mention that the exponent 2 in equation (2-13) is coming from $\frac{1}{0.5}$ and it will change for notches characterized by a stress gradient different from the one characterizing a crack.

$a^{*}= a_0 \, . \, k_t^2$ (2-13)

When the notch dimension is larger than $a^*$ ($a > a^*$), we have blunt notch where peak stress criteria using $k_t$ controls fatigue strength while for notch sizes between $a_0$ and $a^*$ ($a^* > a > a_0$), the stress field criteria influences the fatigue life.

In summary, Atzori et al. [43, 44] attempted to provide a unified design approach for assessing the fatigue strength in the presence of defects and notches characterized by notch stress intensity factor. The NSIF is dependent on the stress distribution of notch and it is changed for blunter notches. Therefore, the A-L diagram in Figure 2-14 transforms to Figure 2-15 by variation of notch dimensions at constant acuity. In this condition, the slope of the diagram ($\alpha$) changes and the $\Delta K_{th}$ is substituted by the threshold stress intensity factor range of the notch $\Delta K_{th,n}$ (MPa.m$^{\alpha}$) that could be determined experimentally. In addition, the $a_0$ and $a^*$ are changed as $a_{0,n}$ and $a_n^*$, respectively and they are determined as follows:

$$a_{0,n} = \left(\frac{\Delta K_{th,n}}{\sqrt{\pi}\,\Delta\sigma_0}\right)^{\frac{1}{\alpha}} \quad (2\text{-}14)$$

$$a_n^{*} = a_0 \, . \, k_t^{\frac{1}{\alpha}} \quad (2\text{-}15)$$

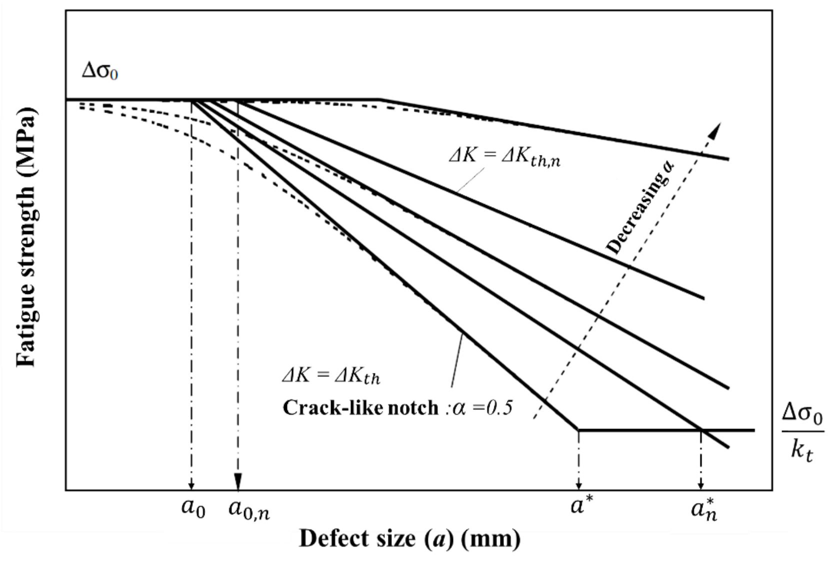


Figure 2-15 Generalized Atzori-Lazzarin diagram at constant $k_t$. [modified from [43, 44]].

To give an example, Atzori et al. [42], presented the fatigue strength variation as a function of notch depth for welded aluminum alloy tested at $R$= 0.1 and 2*10$^6$ cycles in Figure 2-16. The test specimens have lateral V-notch. The transition points of $a_{0,n}$ and $a_n^*$ are shown by the dotted lines. The $\alpha$ and $\Delta K_{th,n}$ for this notch determined by the equation of the line fitted on the experimental results are equal 0.326 and 92.5 MPa.mm$^{0.326}$, respectively. In such a case, using a LEFM approach would result in an underestimation of the fatigue strength as shown by the orange line, schematically.

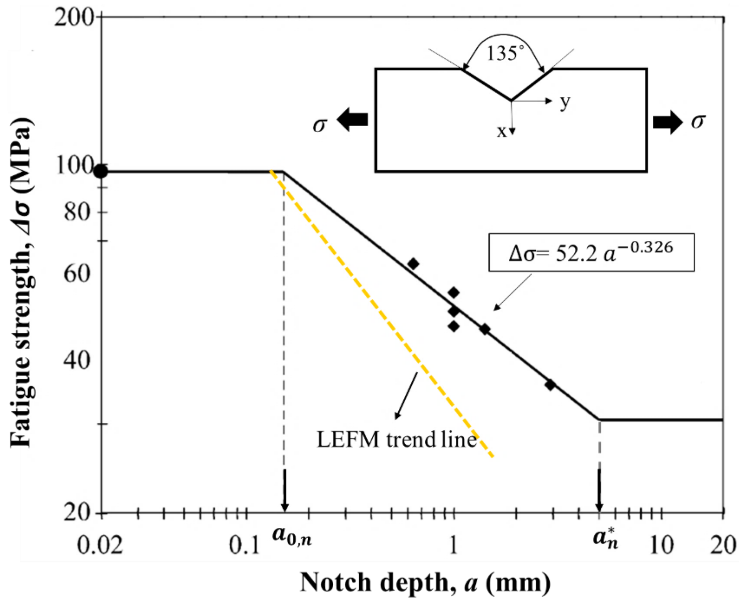


Figure 2-16 Atzori-Lazzarin diagram for welded notched aluminum alloy at *R*=0.1 and *N*= 2*10$^6$ cycles [42].

## 2.3 Summary of literature and problem definition

According to the literature review, previous research has demonstrated that multipass welds of 410NiMo steel typically contains various discontinuities, such as lack of fusion, non-metallic inclusion, porosity, and lack of penetration. The inclusions are mainly composed of oxides of Al, Zr, Ti, and Si and have a rounded shape with an average diameter size of 5-10 µm. The porosities can be quite large, extending through the thickness by a few millimeters. Meanwhile, the lack of fusions have irregular shapes with sizes of approximately 500 µm and are considered as crack-like defects.

These defects are a result of the welding process, and based on their shape, size and geometry, they can be considered as cracks or notches. Atzori and Lazzarin provided a general diagram that works for different geometries of discontinuities with similar acuity and shows the influence of discontinuities on the fatigue strength. This diagram has a transition size, *a**, from the zone governed by the stress field to the zone controled by the peak stress at specific $k_t$ and $\alpha$. Their study reveals that if a discontinuity size is larger than the transition size, it behaves like a blunt notch. The tools used to predict fatigue strength are material dependent. To the author's knowledge, there is no published A-L diagram calibrated for the 410NiMo welded material. It is therefore uncertain which approach between LEFM or notch approaches is more accurate to predict the fatigue strength of hydroelectric turbine runners in the presence of discontinuities with rounded or elliptical shape. Accordingly, the research question below has been formulated to provide solutions to the identified challenges:

*"Could the use of notch approaches improve the accuracy of the fatigue strength prediction for welded turbines?"*

## 2.4 Objectives

The under listed objectives of this project have been developed to scientifically provide answers to the aformentioned research question.

1) Predict the transition conditions from LEFM to the notch theory for 410NiMo welds.
2) Experimentally validate the predictions.
3) Improve the accuracy of the K-T design tool by incorporating the notch approach.

# CHAPTER 3 MATERIALS AND METHODS

The correlation between the methodology and the project objectives is given in Table 3-1. The first task involves the manufacture of the weld, its microstructural characterization and preparation of fatigue specimens. Subsequently, the focus shifts to the design of artificial notches that will be used to simulate the presence of discontinuities. In this step, the Abaqus CAE software is utilized for FE simulation, enabling the determination of the $k_t$ and stress gradient around the notch. By incorporating numerical simulation results and information gathered from a literature review, the appropriate sizes of the notches required on the fatigue samples are determined. Then, through the fatigue test results and analysis of the fatigue samples using fractography, the second objective is successfully achieved. Finally, by comparing the fatigue results from experimental tests with the predictions, an improved design tool will be provided.

Table 3-1 Methodology and research plan based on the objectives.

| **Methodology** | | **Objectives** | | |
|---|---|---|---|---|
| **Tasks** | **Test method** | **1. Predict the transition conditions from LEFM to the notch theory for 410NiMo welds.** | **2. Experimental validation of the predictions.** | **3. Improve the accuracy of the design tool by incorporating the notch approach.** |
| **1.1** Manufacture and microstructure characterization of the weld | FCAW, PWHT, microstructure characterization by OM, SEM, EDS, XRD. Tensile and hardness test. | **X** | **X** | **X** |
| **1.2** Characterize the geometrical features ($k_t$, $\alpha$ and stress field) of natural discontinuities | FEA by Abaqus CAE | **X** | | **X** |
| **1.3** Estimate the transition size between long cracks and notches based on literature data and FEA. | Microdrilling, heat treatment, polishing and preparation of notched specimens. | **X** | | **X** |
| **2.1** Produce artificial defects with characteristics comparable to the natural defects. | | **X** | **X** | **X** |
| **2.2** Fatigue tests of smooth and notched specimens. | Step method @$R$= 0.1, $N$= 2*$10^6$ | | **X** | **X** |
| **2.3** Observe fractographies | OM, SEM, EDS, XRD | | **X** | **X** |
| **3.1** Compare experiments and predictions to calibrate a design tool | **-** | | | **X** |

Detailed discussions about the experimental techniques and material analyses will be presented in the subsequent sections.

## 3.1 Manufacture of the weld

To deposit the weld beads on the 415 stainless steel base material, the FCAW technique was employed. The flux-cored wire of ER410NiMo was used as the filler material. The welding process was done in accordance to the AWS A.5.22 [16] by the industrial partner at IREQ. Detailed information regarding the welding parameters can be found in Table 3-2. Fast heating and cooling occurring during the welding operation results in residual stresses in the part. Therefore, a stress relief post weld heat treatment was performed at 605± 5 ˚C for 8 hrs.

Table 3-2 FCAW welding parameters.

| **Method** | Preheat temp(˚C) | Inter-pass temp(˚C) | Voltage (V) | Current (A) | Torch speed (mm/s) | Deposition rate (kg/h) | Heat input (J/mm) | Welding position | Gas |
|---|---|---|---|---|---|---|---|---|---|
| **FCAW** | 100 | 160 | 28.4 | 268 | 6.5 | 5 | 1171 | 1G | Ar-25% $CO_2$ |

## 3.2 Characterization of welded 410NiMo material

Specimens were drawn from the welded part and characterized to check for conformance to the ER410NiMo reference standard AWS A5.22. The following sections provide further details on the studied characteristics.

### 3.2.1 Chemical composition

The chemical composition of the welded material in %wt. and the A.5.22 specifications are provided in Table 3-3. Oxygen stream combustion-infrared absorption method was used for carbon and sulfur analysis while glow discharge optical emission spectroscopy (GDS) was used for other elements. All elements, except for nickel, are within specified ranges for a 410NiMo filler material. It can be seen that the %wt. of nickel is higher than the standard value.

Table 3-3 Chemical composition of the welded 410NiMo material (%wt.).

| | C | Mn | P | S | Si | Cr | Ni | Mo |
|---|---|---|---|---|---|---|---|---|
| **ER410NiMo** | 0.025 | 0.34 | 0.018 | 0.009 | 0.5 | 11.7 | 5.32 | 0.66 |
| **ER410NiMo [16]** | < 0.06 | < 1.0 | <0.04 | <0.03 | < 0.5 | 11.0-12.5 | 4.0-5.0 | < 1.0 |

### 3.2.2 Microstructural characterization

Three welded samples were extracted from central parts of the heat-treated block in the weld zone for microstructural analysis as shown in Figure 3-1. The samples were mounted with hot mounting and subsequently grinded using SiC paper of varying grit sizes ranging from 240 to 1200 µm. They were then polished with diamond suspension with particle sizes of 6, 3, and 1 micron. Thereafter, the specimen was etched using Kalling's reagent #2 (2 gr $CuCl_2$ + 40 ml HCl + 40 ml ethyl alcohol) as recommended in ASTM E407[45].

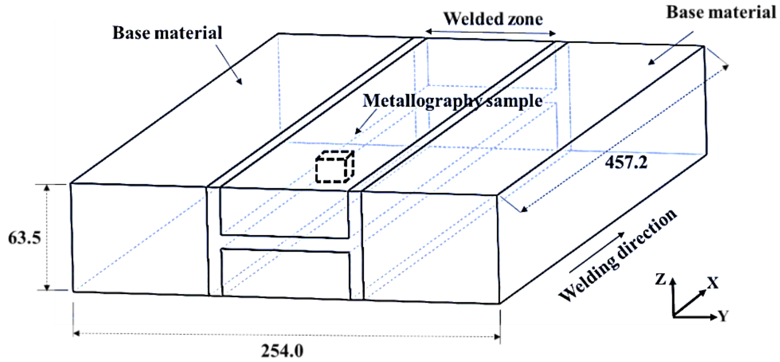


Figure 3-1 Schematic of the welded block and the extracted sample for microstructural characterization (all dimensions are in mm).

### 3.2.3 Mechanical characterization

The micro-hardness evaluation was carried out using the Akashi setup by 300 gf in accordance with the ASTM E384[46]. For the tensile test, three sub-sized tensile specimens with 4 mm diameter designed according to ASTM E8 [47], and were tested to determine the mechanical properties of the material. These samples were extracted from the weld zone to ensure the failure location in the weld material. Figure 3-2 shows the schematic view of the extraction pattern. The technical drawing is provided in Annex A.

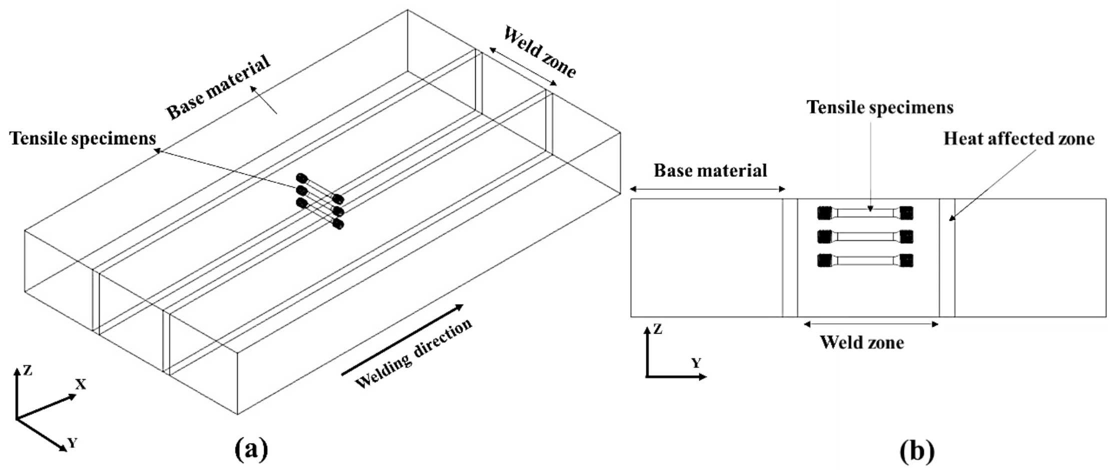


Figure 3-2 Schematic presentation of the extracted tensile test specimen from the welded block in (a) isometric view and (b) front view.

The three tests were conducted under ambient atmospheric conditions using Instron 1362 frame of MTS Renew controller with a 20 kN load cell. An MTS extensometer 634.11F.24 with a gauge length of 25 mm attached to the sample for purpose of elongation measurement. The maximum engineering stress was considered as the ultimate tensile strength ($\sigma_{UTS}$) and the yield strength ($\sigma_Y$) was calculated by the 0.2% approach in accordance with ASTM E8.

## 3.3 Predicting the transition conditions

### 3.3.1 Geometrical features of discontinuities and stress fields

Geometrical features of natural discontinuities are characterized by the stress concentration factor $k_t$, stress field size and singularity exponent $\alpha$. Determination of the stress concentration of discontinuities in the material helped to establish the transition conditions in the A-L diagram. Thus, considering a simplified case of hemispherical discontinuity, FEA analysis was carried out to simulate the stress concentration.

The finite element simulation by Abaqus CAE software for the elastic stress distribution around the notches was performed using these material features: Young's modulus 200 GPa, Poisson ratio ($\upsilon$) =0.3. A rectangular model having the gauge section with dimension of the real fatigue specimen with a hemispherical notch in the center of the front face was used for the simulation. The half of above mentioned cube was simulated using X- symmetry (see Figure 3-3) to reduce the number of elements and simulation time. The cube was fixed in Y- direction as well while the nominal stress of 1 MPa was applied on the top surface in Y-direction as shown in Figure 3-3.

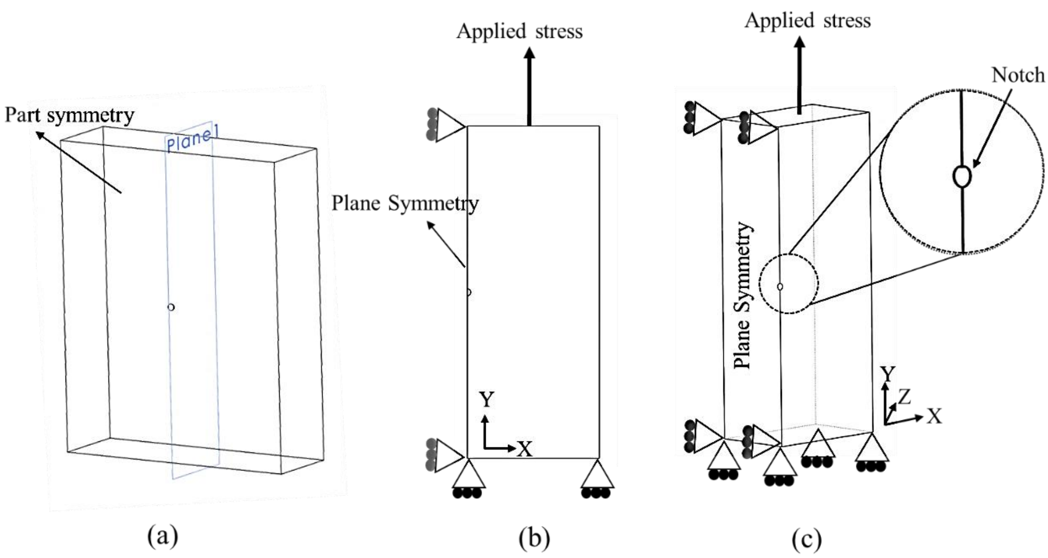


Figure 3-3 (a) Complete model and (b,c) boundary conditions of notched component with applied stress of 1 MPa.

In this model, the coarse Hex mesh with the size of 0.3 mm was employed while finer mesh size of 0.02 mm was used for notch and close areas around it to characterize the stress distribution around the notch. It worth to mention that meshing convergence around the notch with 5% criteria was done in order to be sure that the mesh size does not affect the final results. As shown in Figure 3-4, the $\sigma_{local}$ at the tip of the notch in X or Z direction gives the stress concentration factor. Since the nominal stress is equal to one, the $k_t$ is equal to the maximum $\sigma_{local}$. The slope of this curve is the singularity exponent of notch ($\alpha$) which is a function of notch geometry and its maximum value is equal to 0.5 for crack-like discontinuities [48].

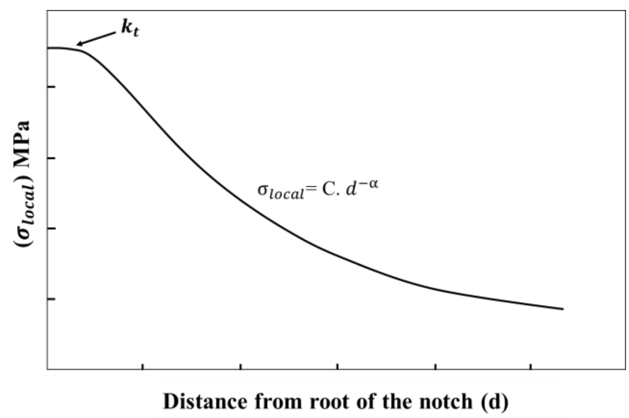


Figure 3-4 Schematic of stress distribution around a hemispherical notch ($\sigma_{nominal}$ = 1 MPa) in Z or X direction.

## 3.4 Experimental fatigue tests

### 3.4.1 Transition points

As mentioned in section 2.4.5.1, there is a lack of information for notched 410NiMo welded material. In order to estimate the crack size limiting the different regions of the A-L diagram, we can use $k_t$, $\Delta K_{th}$ and $\Delta\sigma_{a,0}$ from the literature information for $\alpha$= 0.5. As shown in Figure 3-5, the $\Delta K_{th}$ for welded 410NiMo material with a crack-like notch with singularity exponent of 0.5 is equal to 5.16 MPa.$\sqrt{m}$ at R= 0.1 [49]. We can assume that the fatigue limit of the material is equal to 240 MPa at R= 0.1 [23] although we know that the failure occurred from the discontinuity. This value was calculated employing Goodman equation [29] for the result of fatigue test on 410NiMo material at R= -1. Also, if the discontinuities or notches are circular and blind, the $k_t$ is equal to 2 [32]. According to these information, the transition points of $a_0$ and $a$* are equal to 0.035 and 0.14 mm when $\alpha$ is equal to 0.5. Considering the transition points and limitations of micro drilling tools, we choose to produce notches with acuity of one and radii 0.2, 0.5, 1 and 2 mm larger than predicted $a$* in the blunt notch zone.

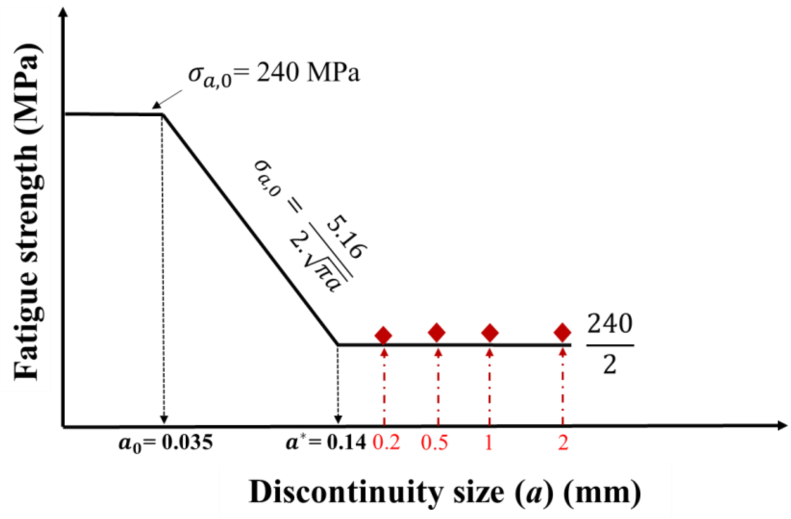


Figure 3-5 Predicted Atzori-Lazzarin diagram for welded 410NiMo at R=0.1 to design the notch dimensions.

### 3.4.2 Sample preparation

In order to have a failure in the weld material, the gauge section of the fatigue specimens was completely extracted from the welded zone, as illustrated in Figure 3-6. The extraction of fatigue specimens from the welded zone was done in a way to be coherent with the actual mechanical loading of the welded turbine assembly.

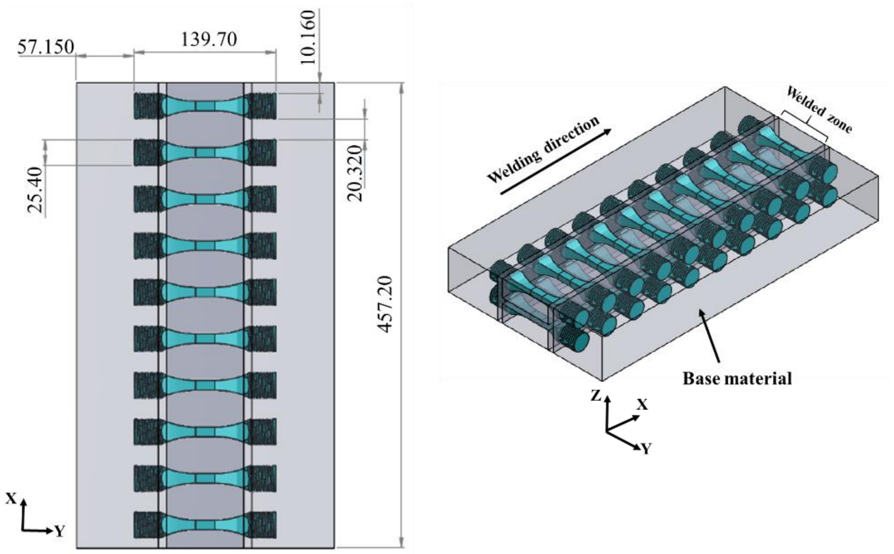


Figure 3-6 Schematic view of the fatigue samples extracted from a unique welded block (all dimensions are in mm).

Figure 3-7 gives the dimensions of smooth fatigue specimens which were designed in accordance with ASTM E466 [27]. The detailed drawing is provided in Annex A.

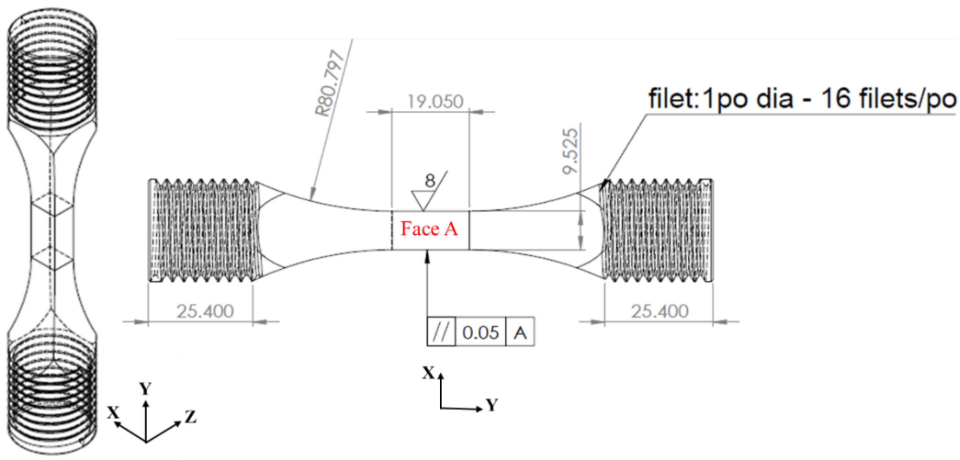


Figure 3-7 Manufacturing drawing of the fatigue specimens (all dimensions in mm).

Figure 3-8 illustrates the schematic of fatigue specimen with a hemispherical notch on the surface. The artificial notch was manufactured on Face A (see Figure 3-8) in order to have crack initiation and propagation perpendicular to the direction of weld beads. The dimensions of specimens with and without notch are identical. All fatigue specimens were polished using SiC paper of varying grit sizes ranging from 240 to 1200. They were then further polished with diamond suspension containing particles that were 6, 3, and 1 micron in size.

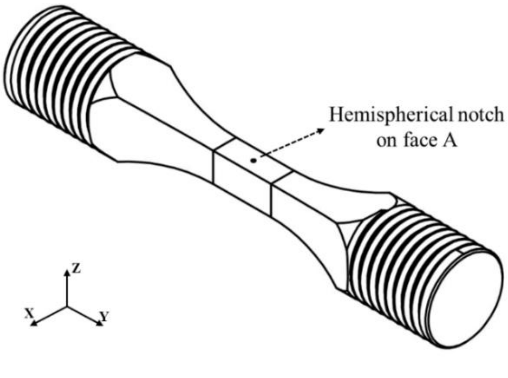


Figure 3-8 Schematic of notched specimen in isometric view.

### 3.4.3 Manufacturing and characteritics of notches

**Drilling method**

According to estimated values of $a_0$ and $a^*$ and limitations of the micro drilling tools, we choose to produce notches with an acuity of one. The micro drilling was done using the flange motor spindle with model of BM-319F. The machine had the 80000 rpm rotation speed with spindle accuracy of 1 µm. The size of notches was quality controlled by topographic measurements.

**Microstructure characterization after micro drilling**

To ensure that the micro drilling process does not affect the initiation and propagation of cracks in notched specimens, an additional heat treatment was carried out to release any potential residual stresses around the notch. This involved subjecting sample to a temperature of 475 °C for a duration of 2 hours. After the second heat treatment, no measurements of the residual stress were performed and we made the hypothesis that it was completely released. Also, the microstructure characterization was performed in order to study the micro drilling in different distances around the notch.

Knowing that the austenite is subjected to plasticity induced phase transformation, the microstructure around the notch was examined. In order to measure the austenite content, the samples were polished using SiC paper ranging from 240 to 1200 grit. Then, chemical polishing was performed to get rid of at least 50 microns of the surface of each sample. This was done to ensure that any material layer that could have been affected by mechanical polishing was removed. Next, the samples were placed in an agitated solution of HCl, $HNO_3$, and $H_2O$ for ten minutes, and then rinsed with water and ethanol. Quantitative X-ray diffraction was carried out at IREQ, using a Bruker D8-Advance diffractometer equipped with a Cu tube with an Ni filter, at a voltage of 25 kV and current of 20 mA. Scanning angles were 2θ = 40° to 140° in 0.05° steps, at a duration of 3-4 seconds on rotating samples. Finally, the Rietveld analysis with Topaz software was used to determine the amount of austenite phase present in the microstructure. As shown in Figure 3-9, the XRD scanning with two repetitions were taken at two different distances from the notch.

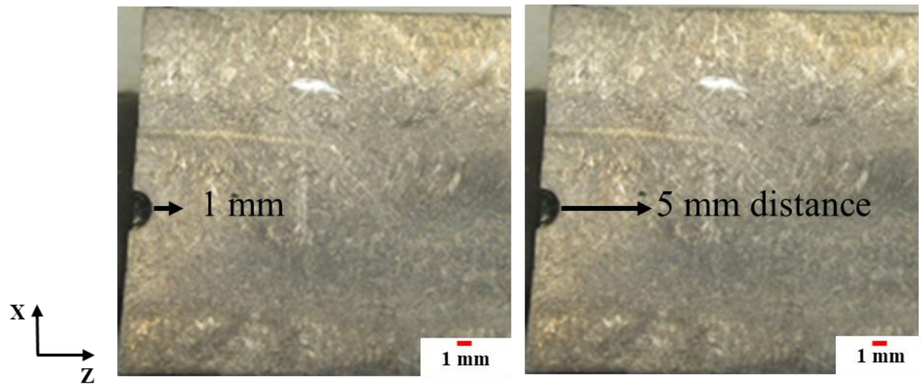


Figure 3-9 Location of austenite measurement of 415 stainless steel (a) close and (b) 5 mm away from the notch.

**Hardness measurement after micro drilling**

The hardness of the material around the notch was measured using the Hysitron Ti 950 Tribo Indenter Bruker. All tests were performed by a Berkovich tip and a load of 5000 µN. As shown in Figure 3- 10, for each of the sets of results, a 3 × 3 matrix of indentations was performed in different distances and angles around the notch, for a total of 9 repetitions, and the average contact depth across all results was 175 nm. For instance, 45-50 µm means that the nano indentation was done in angle of 45 degree and distance of 50 µm from the notch.

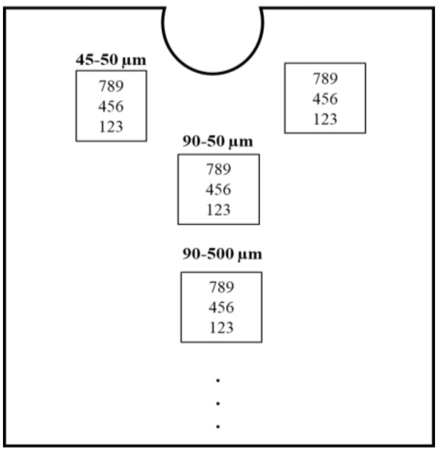


Figure 3- 10 Schematic of nano indentation test around the notch.

### 3.4.4 Fatigue test

The axial fatigue tests were conducted at $R$= 0.1 and targeting a number of cycles $N$= $2*10^6$ cycles using the Vibrophore machine model 200 HFP 5100. The test frequency was approximately 105 Hz. The fatigue tests were performed using the step method proposed by Maxwell and Nicholas [50]. Figure 3-11 schematizes the test procedure. To start the test for smooth specimen, the stress level of the initial step must be smaller than the fatigue strength of material at $2*10^6$ cycles. If the material withstands this number of cycles without failure, the stress level is elevated by 20 MPa and the process is repeated for the same number of cycles again. This process continues until failure occurs at step "$n$" after "$N_f$" cycles, which is less than 2 million cycles. In order to account for the fatigue damage of previous steps, the fatigue strength ($\sigma_a$) at $2 \times 10^6$ cycles is determined by equation (3-1).

$$\sigma_a = (\sigma_{a,n} - \sigma_{a,n-1}) \times \frac{N_f}{2 \times 10^6} + \sigma_{a,n-1} \tag{3-1}$$

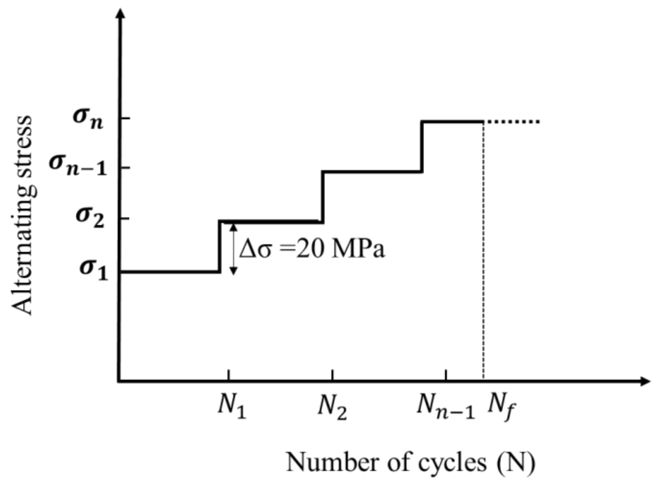


Figure 3-11 Schematic view of step-loading procedure used by Maxwell and Nicolas for fatigue test if $N_1$= $2\times10^6$ cycles.

The fracture surface analysis was conducted through the use of optical microscopy (OM) and scanning electron microscopy (SEM). The dimensions of discontinuities at the crack initiation sites are measured in terms effective area ($\sqrt{area}$) and diameter using ImageJ software. For sub-surface discontinuities, the maximum distance from the surface is equal to the diameter of discontinuity. For internal discontinuity, we consider a circular area having diameter equal to the major axis of discontinuity. Figure 3-12 illustrates the method for measuring the size of internal and subsurface discontinuities. In order to measure the size of surface and sub-surface discontinuities in real cases during service of turbine runners, non-destructive testing methods (NDT) are used by industrial partner.

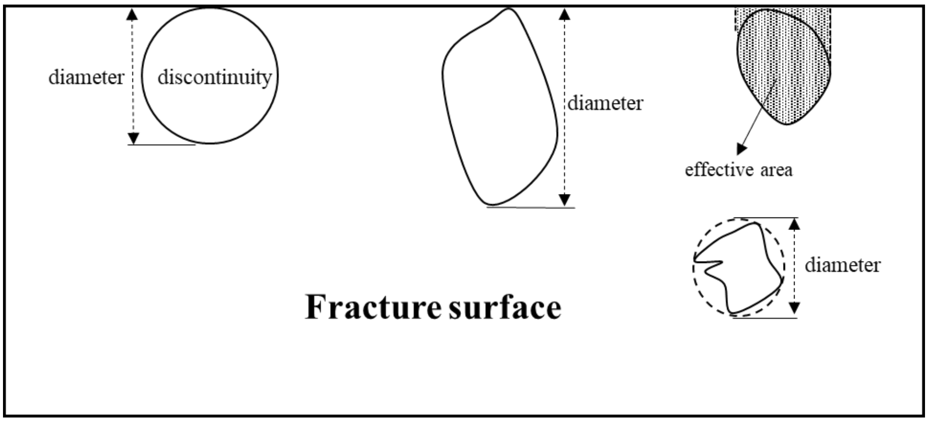


Figure 3-12 Measurement of diameter and area of discontinuities on the crack initiation sites.

In summary, Table 3-4 provides an overview of the experimental tests of the project, including the number of samples for each test.

Table 3-4 Summary of the experimental tests.

| | **Metallography** | | | **Tensile test** | **Hardness test** | **Fatigue test and fractography** | | | | |
|---|---|---|---|---|---|---|---|---|---|---|
| | OM, SEM (microstructure) | XRD (austenite%) | GDS (chemical composition) | | | Smooth | Notched | | | |
| | | | | | | | $a_1$ | $a_2$ | $a_3$ | $a_4$ |
| **Sample** | 4 | 2 | 2 | 3 | 2 | 2 | 6 | 4 | 4 | 4 |
| **Measurements** | 4 | 4 | 1 | 3 | 4 | 2 | 6 | 4 | 4 | 4 |

# CHAPTER 4 RESULTS AND DISCUSSION

This chapter starts with the material characteristics of welded 410NiMo material and effect of notch manufacturing on the material properties around it. Then, the results of finite element analysis, which aimed to investigate the stress distribution surrounding notches are presented. Through the FEA, the $k_t$ and $\alpha$ for notches with constant acuity are successfully determined. The subsequent section provides the empirical fatigue test results, accompanied by fractographic observation obtained from both smooth and notched specimens. Employing these experimental data, we attempted to provide an accurate design tool for welded 410NiMo material, considering the effect of discontinuities and notches on the fatigue strength. Lastly, a comparative examination between experimental data and outcomes derived from the theory of critical distance adds a further understanding to our analysis.

## 4.1 Material characteristics of welded 410NiMo

### 4.1.1 Microstructural features

Figure 4-1 shows the martensitic microstructure of the welded material. Regions with columnar shape and fine martensitic grains are distinguished in Figure 4-1(b). The columnar microstructure is the result of the heat flow and solidification direction during welding. The fine grain martensite microstructure is at the boundary between two weld beads where the temperature is raised to cause grain recrystallization.

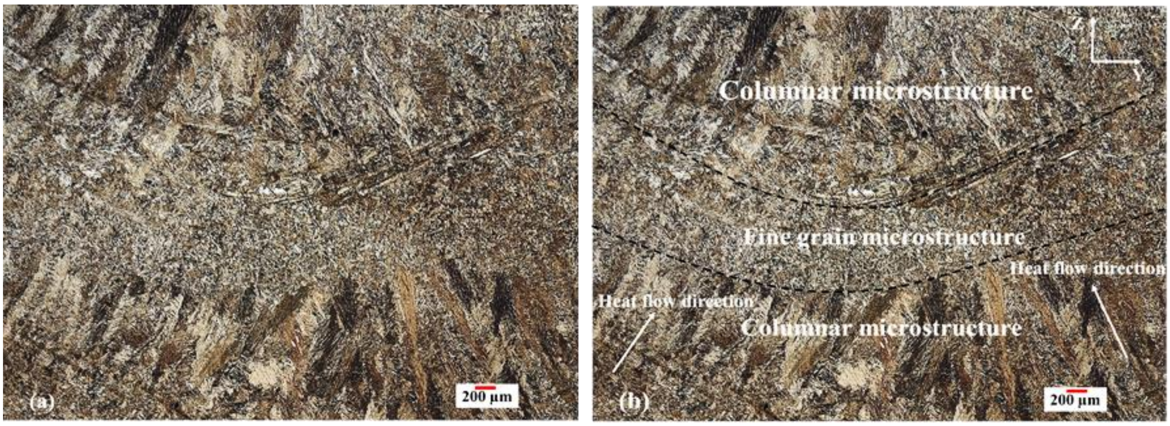


Figure 4- 1 (a) Microstructure of the multipass weld etched with Kalling's No.2 perpendicular to the welding direction, (b) dotted lines show the boundaries between columnar and fine grains.

### 4.1.2 Mechanical properties

Table 4-1 gives the results of micro hardness and tensile tests. The average hardness of the material is 298 HV ± 8. This hardness value is consistent with the hardness values reported by Amrei et al.[51] and close to that of the 415 stainless steel base material [52]. Comparing the experimental results of tensile test with the standard, the ultimate tensile strength is within the standard requirement but the elongation to fracture is lower than the required value of 15 %. This difference is attributed to the applied heat treatment and natural discontinuities in the welded material. For instance, larger weld discontinuities cause the reduction of $e_f$ (%).

Table 4- 1 Average mechanical properties of the welded 410NiMo material.

| Material | (0.2%) $\sigma_Y$ (MPa) | $\sigma_{UTS}$ | $e_f$ (%) | Hardness *(HV)* |
|---|---|---|---|---|
| 410NiMo-HT | 680 ± 20 | 825 ± 22 | 11 ± 2.5 | 298 ± 8 |
| AWS A5.22 (min) [16] | - | 760 | 15 | - |

## 4.2 Material characteristics around notches

### 4.2.1 Topography results

Figure 4-2 shows the topography results for notch depth of 0.2 mm. The dimensions of all notches after topography are summarized in Table 4-2. Although the acuity of notches may not be equivalent to one, its effect on the variation of the $k_t$ value is ignored.

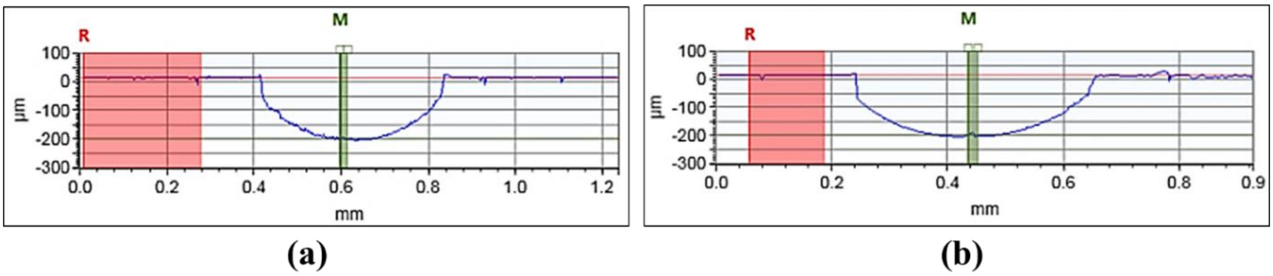


Figure 4- 2 Topography results of notch depth of 0.2 mm (a) X profile and (b) Y profile.

Table 4- 2 Topography results of notched components.

| $a = \rho$ (mm) | Measured $a$ (X-profile) (mm) | Measured ρ (mm) | Measured $a$ (Y-profile) (mm) |
|---|---|---|---|
| 0.2 | 0.21 | 0.21 | 0.22 |
| 0.5 | 0.48 | 0.54 | 0.45 |
| 1 | 1.02 | 0.98 | 1.19 |
| 2 | 1.9 | 2.06 | 1.98 |

### 4.2.2 Material characterization around the notch

In order to study the effect of micro drilling, the microstructure characterization around notches was performed on the 415 stainless steel. Figure 4-3 shows the microstructure with different distances from the notch with depth of 2 mm as the largest notch. It can be seen that the martensitic microstructure in different distances from the notch does not change. In addition, the austenite percentage close to the root of the notch and in 5 mm distance is equal to 16.5% and 20.5%. As reported by Chaix [53], the maximum standard deviation of austenite content for this material is 8%.

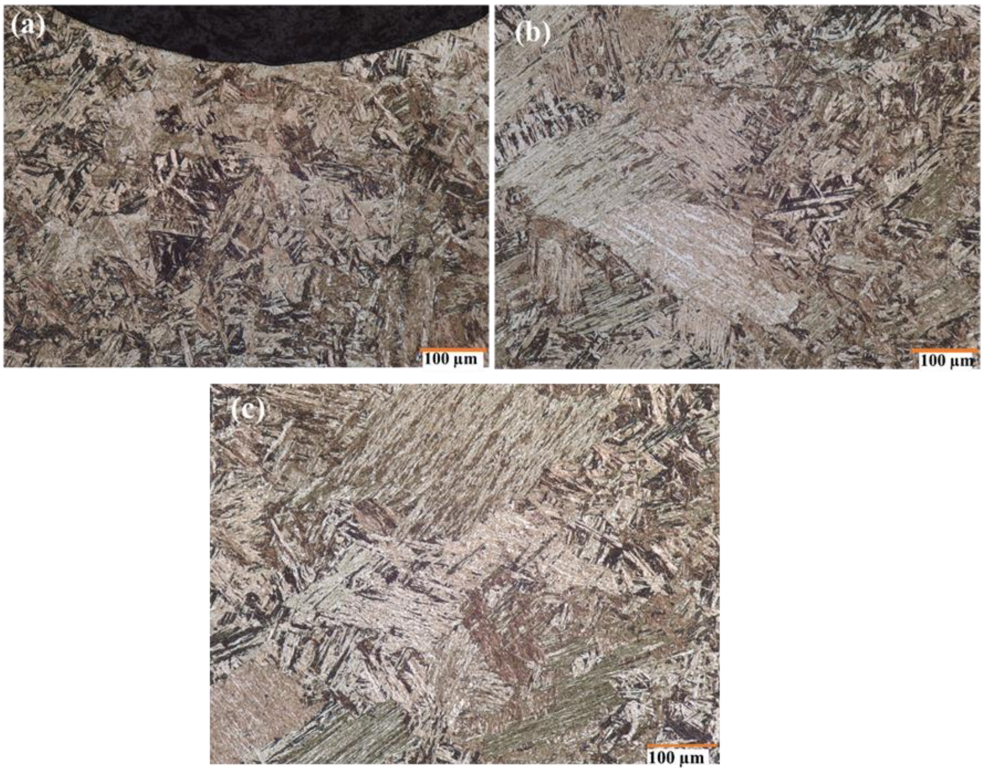


Figure 4- 3 Microstructure characterization on the 415 stainless steel (a) in the vicinity of the notch, (b) 1 mm away from the root, (c) 2 mm away from the root of notch.

The nano indentation results in Table 4-3 showing that the hardness around the notch in different distances is in the range of 4.71 ± 0.16 GPa. According to this table, the hardness data exhibits a negligible standard deviation of 0.17, indicating a small decreasing of hardness in larger distances from the notch that can be disregarded in our analysis.

Table 4-3 Results of nano indentation test around the notch.

| **Angle (degree)** | **Distance from the notch (μm)** | **Avg. Hardness (GPa)** |
|---|---|---|
| **45** | 50 | 4.83 ± 0.04 |
| **135** | 50 | 4.89 ± 0.27 |
| **90** | 50 | 4.79 ± 0.08 |
| **90** | 500 | 4.74 ± 0.33 |
| **90** | 1000 | 4.65 ± 0.23 |
| **90** | 2000 | 4.36 ± 0.16 |
| **90** | 4000 | 4.77 ± 0.22 |

## 4.3 Numerical results by finite element analysis

The results of finite element simulation of elastic stress around the artificial notch is shown in Figure 4-4. The maximum local stress in Y direction ($\sigma_{yy}$=$\sigma_{local}$) is equal to 2 MPa when applying a $\sigma_{nominal}$ of 1 MPa for the notch radius of 0.2. Therefore, the $k_t$ of this notch is equal to 2. Figure 4-4 (b) illustrates a closer view of the stress distribution around the notch and it can be seen that the highest maximum stress is on the XZ plane perpendicular to the applied load direction. Also, the results of the mesh convergence around the notch is shown in Figure 4- 5. It can be seen that by decreasing the mesh size (from 0.3 to 0.02 mm), the number of element increases and the $\sigma_{local}$ converges to 2 MPa.

Figure 4-6 illustrates the stress distribution as a function of distance from the root of the notch along the Z and X direction. It can be seen that the $k_t$ for notches with $\zeta$ = 1 is equal to 2 at the root and it decreases to 1 at distances far from the notch. Slope of the curve gives singularity exponent ($\alpha$) equal to 0.16 which is different from the 0.5 value expected for crack-like notches. As the crack can propagate in multiple directions, the value of $\alpha$ exponent is established as 0.2 using the stress gradient in the X direction, following a similar finite element analysis approach as applied to the Z axis. The $\alpha$ exponent in X direction is higher than in Z direction because there is plane stress condition on XY plane. The FEA results for notch radiuses of 0.5, 1.0 and 2.0 mm were similar to Figure 4-4 and Figure 4-6 because the acuity remains constant.

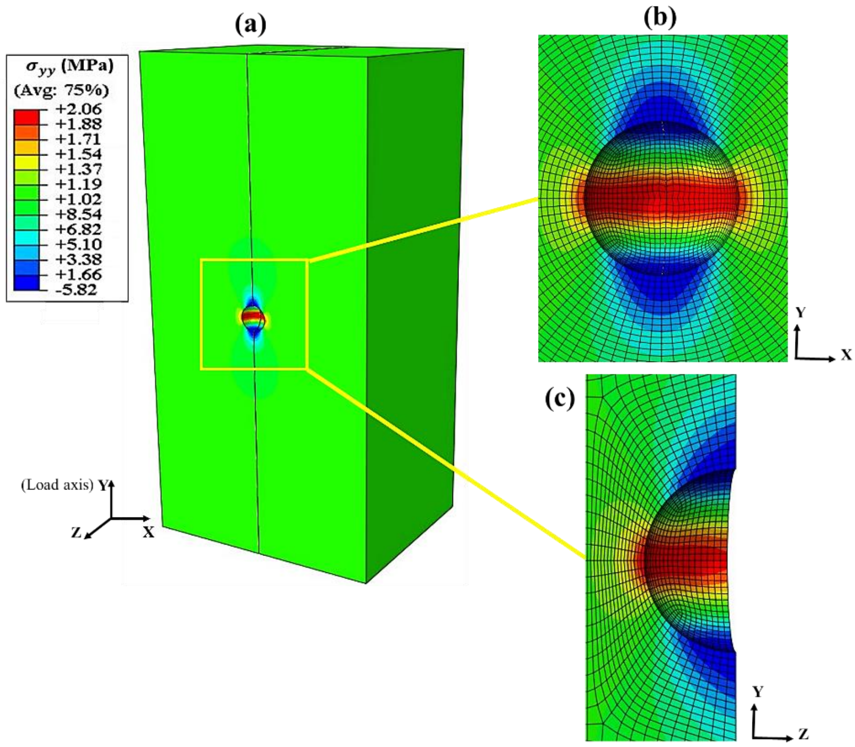


Figure 4-4 Modelling and stress distribution around the hemispherical notch of depth 0.2 mm in (a) isometric view, (b) front view and (c) side view (half the model).

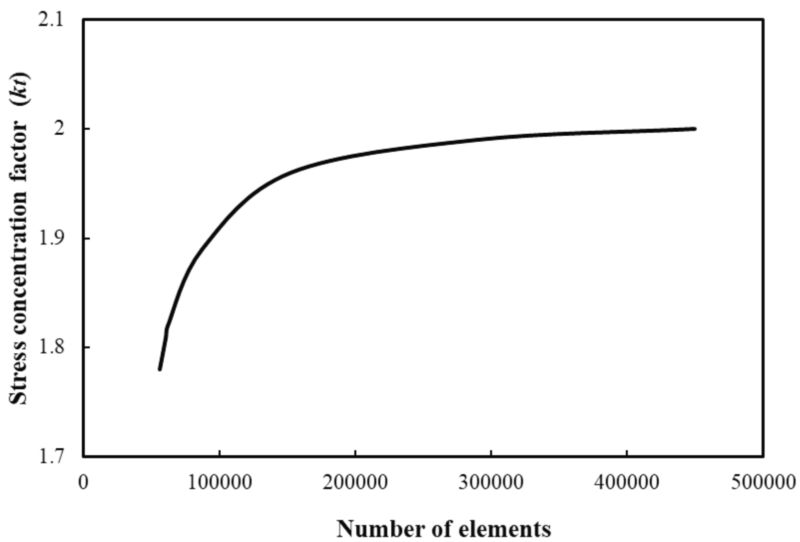


Figure 4- 5 Mesh convergence around the notch.

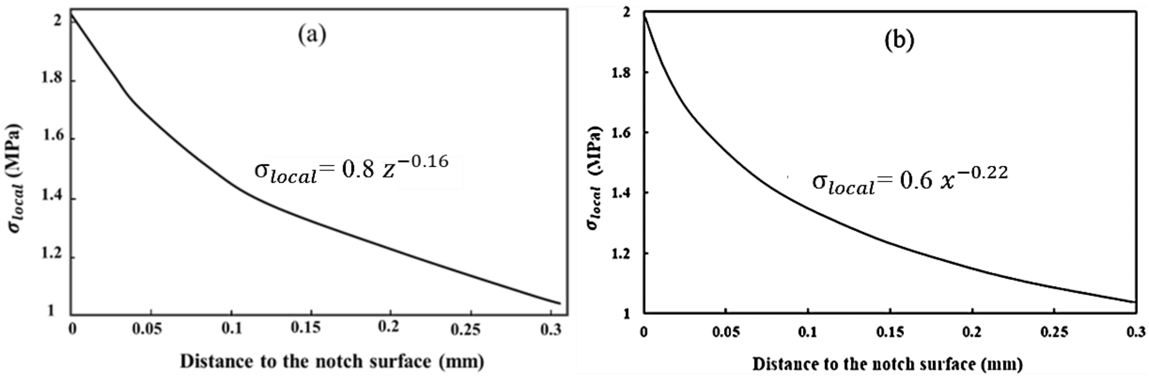


Figure 4-6 Stress gradient in (a) (Z-axis) and (b) X-axis around the notch radius of 0.2.

In order to compare the limit of the notch stress field, the stress distribution versus distance from the root of the notch with depths of 0.2, 0.5, 1 and 2 mm (along Z-axis) in log-log scale are illustrated in Figure 4-7. Accordingly, the limit of notch stress field is reached when $\frac{\sigma_{local}}{\sigma_{nominal}}$ =1. It can be seen that by increasing the notch depth, the limit of notch stress field extended further away from the notch. Also, the stress distribution around the notches in X-axis are provided in Annex C. Table 4-4 provides a summary of notch characteristics and FEA results in X and Z direction.

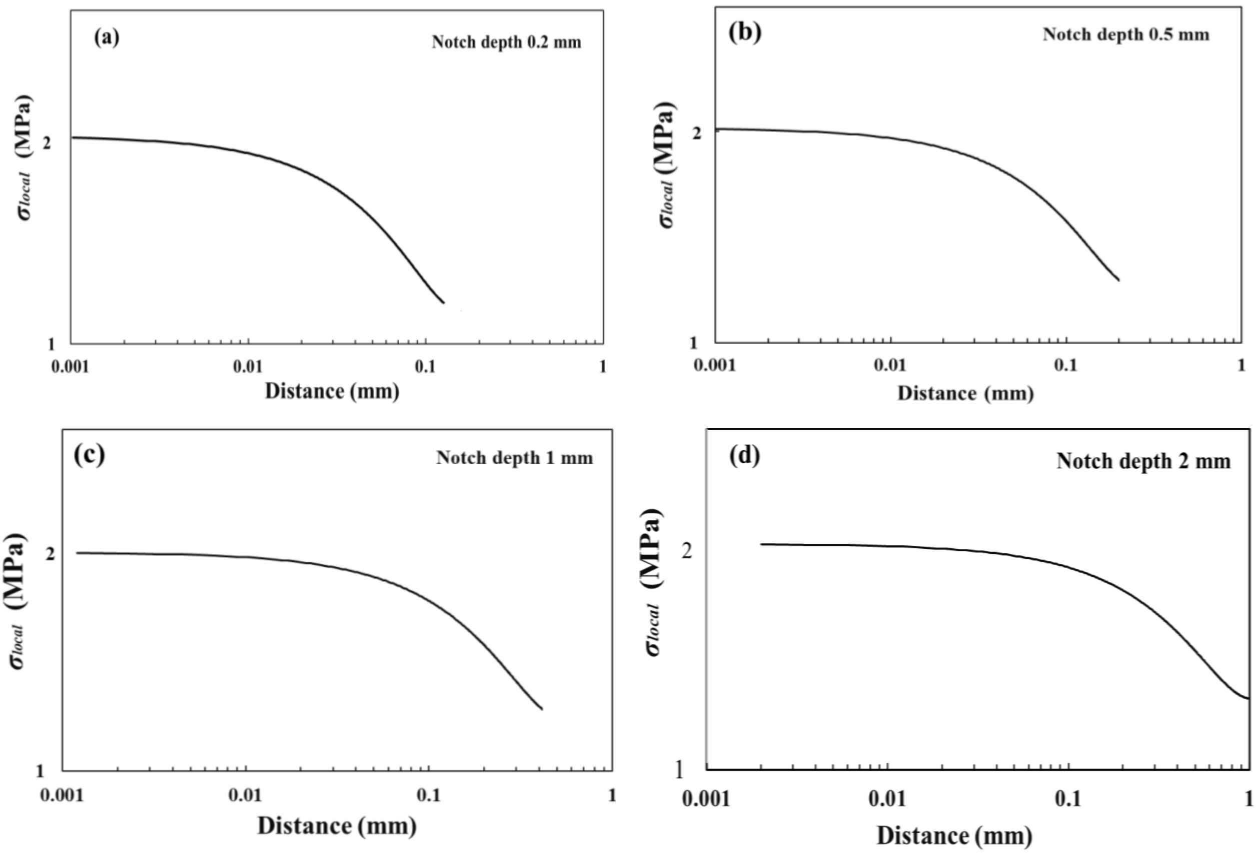


Figure 4-7 Stress gradient curves in Z-axis for notches with radius of (a) 0.2, (b) 0.5, (c) 1.0 and (d) 2 mm.

Table 4-4 Summary of the notch characteristics in Z and X axis.

| No. | **Depth (mm)** | **Radius (mm)** | **Acuity (ζ)** | $k_t$ | ***α (Z axis)*** | ***α (X axis)*** |
|---|---|---|---|---|---|---|
| 1 | 0.2 | 0.2 | 1 | 2 | 0.16 | 0.22 |
| 2 | 0.5 | 0.5 | 1 | 2 | | |
| 3 | 1 | 1 | 1 | 2 | | |
| 4 | 2 | 2 | 1 | 2 | | |

## 4.4 Experimental fatigue tests

The summary of the fatigue test results of heat treated 410NiMo welded material are given in Figure 4-8. This figure displays the fatigue strength of smooth and notched components. In this figure, the box represents the interquartile range of the data and the line in the box is the median. Also, the bar extends from the minimum to the maximum and "×" is the average of data points. When comparing the fatigue results between smooth specimens and those containing notches, several findings are identified. The smooth specimens have the highest average fatigue strength of 241 MPa at $2\times10^6$ cycles that was close to the fatigue resistance of specimens with notch radius of 0.2 mm (230 MPa). Moreover, out of the six specimens with a 0.2 mm notch radius, only two failed due to the presence of the notch, while the other four failed outside the notched region and will be identified NNE for "no notch effect". This suggests that there is a competition between natural discontinuities and the 0.2 mm artificial notch to initiate a crack.

The pronounced dispersion observed for the 0.2 notch sample (NNE specimens) is provoked by one specimen that failed from a large sub-surface natural discontinuity as will be further described in section 4.5.2. If we do not consider this outlier data, it can be seen that the dispersion decreases (see dotted red box) and the fatigue results of NNE specimens is in the range of smooth specimens. The specimens containing notches of 0.5, 1 and 2 mm have a fatigue strength that decreases with an enlargement of the notch size. For these samples, the notch is large enough ($a_2$, $a_3$, $a_4 > a_0$) to have a significant impact on the resistance to fatigue.

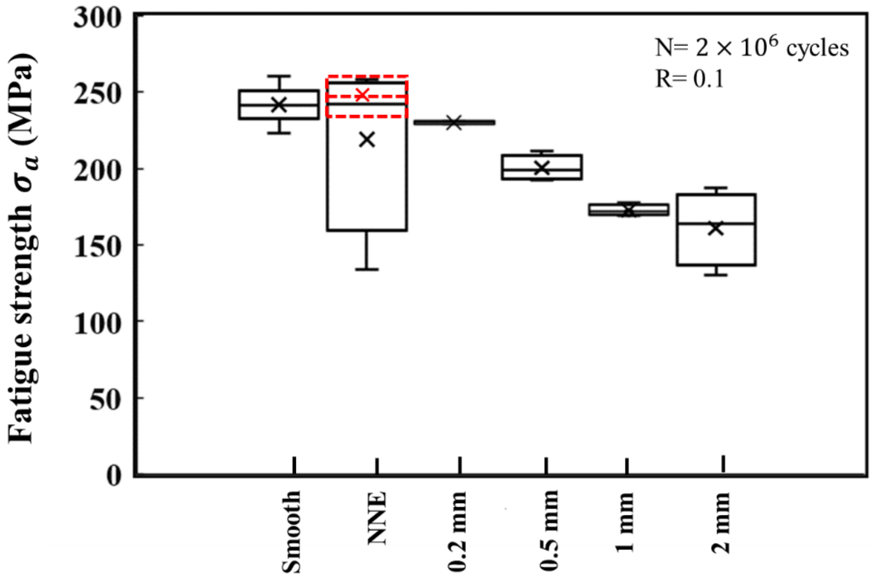


Figure 4-8 The average and range of fatigue strengths of specimens at $R$= 0.1, $N$= 2×10$^6$ cycles.

## 4.5 Fractrographic observation

The summary of experimental fatigue tests including, for each specimen, the fatigue strength, discontinuity size and location at the crack initiation site are given in Table 4-5. Also, the abbreviated names were used for specimens with different notch sizes. For instance, “x” in the name of “Nx-i” means that specimen has a notch with depth of “x”. A specimen identified as "N0-i" as no notch. Also “i” is the number of repetition, i.e. if we have 4 specimens with notch of 0.2 mm, “i” changes from 1 to 4. The nature of the crack initiating feature is also indicated. If the specimen failed from the notch in the presence of oxide inclusion, it is written as “N-oxide inclusion” but if notch does not affect the failure, the type of discontinuity is mentioned only.

The next sections include a two-part analysis of the fracture surfaces. Initially, the fractographic results of two smooth specimens (without notch) are discussed. Subsequently, the focus shifts to the notched specimens in two sub-sections. The first sub-section presents the fracture surface of notched specimens that experienced failure due to the natural discontinuities (NNE) followed by the remaining results.

Table 4-5 Fatigue results, diameter and projected area of discontinuities on the fracture surface.

| Specimen | $a$ (mm) | $\sigma_a$ (MPa) | Initiation type | Discontinuity diameter (µm) | $\sqrt{area}$ $(mm^{0.5})$ | Location | $N_f$ (*$10^6$) |
|---|---|---|---|---|---|---|---|
| N0- 1 | 0 | 260 | Oxide inclusion | 39 | 37 | Sub-surface | 0.23 |
| N0- 2 | 0 | 223 | Oxide inclusion | 100 | 91 | Sub-surface | 0.51 |
| N0.2- 1 | 0.2 | 249 | Mo-rich disco. | 203 | 181 | Internal | 0.34 |
| N0.2- 2 | 0.2 | 258 | Oxide inclusion | 46 | 44 | Sub-surface | 1.21 |
| N0.2- 3 | 0.2 | 235 | Porosity | 70 | 84 | Sub-surface | 0.91 |
| N0.2- 4 | 0.2 | 134 | Mo-rich disco. | 312 | 228 | Sub-surface | 0.82 |
| N0.2- 5 | 0.2 | 231 | N- oxide inclusion | 12 | 10.5 | / | 0.57 |
| N0.2- 6 | 0.2 | 229 | N- oxide inclusion | 18 | 16 | / | 0.31 |
| N0.5- 1 | 0.5 | 201 | N-oxide inclusion | 17 | 15 | / | 1.50 |
| N0.5- 2 | 0.5 | 197 | N-oxide inclusion | 14 | 12.5 | / | 1.14 |
| N0.5- 3 | 0.5 | 210 | N-oxide inclusion | / | / | / | 0.49 |
| N0.5- 4 | 0.5 | 192 | N-oxide inclusion | / | / | / | 0.62 |
| N1- 1 | 1 | 177 | N-oxide inclusion | 15 | 13 | / | 1.18 |
| N1- 2 | 1 | 171 | N-microstructure | / | / | / | 0.54 |
| N1- 3 | 1 | 168 | N-microstructure | / | / | / | 0.28 |
| N1- 4 | 1 | 172 | N-microstructure | / | / | / | 0.60 |
| N2- 1 | 2 | 156 | N-microstructure | / | / | / | 1.01 |
| N2- 2 | 2 | 187 | N-oxide inclusion | 35 | 31 | / | 0.12 |
| N2- 3 | 2 | 171 | N-oxide inclusion | 33 | 29 | / | 0.50 |
| N2- 4 | 2 | 130 | N-oxide inclusion | 37 | 33 | / | 0.41 |

N0: smooth specimen without notch.
N*x*: notched specimen with depth of *x* mm.
$\sigma_a$: Fatigue strength determined by Eq. (3-2).
$a$: notch depth.
N-oxide inclusion: crack initiation from oxide inclusion in the vicinity of the notch.
N-microstructure: crack initiation from microstructure without discontinuity around the notch.
$N_f$ = number of cycles for last step.
If failure occurred from discontinuity in the vicinity of the notch, size of discontinuity is not reported in the table (the symbol / is used).

### 4.5.1 Smooth specimens

Both smooth specimens (N0-1 and N0-2) without artificial notches had crack initiation from a subsurface inclusion (see dotted arrows end to the inclusions on fracture surfaces in Figure 4-9 and Figure 4- 10 ). As shown Figure 4-9, these rounded inclusions are oxides riched in Zr, Ti and Si. The Si is found in the composition of the filler material but Zr and Ti are coming from the flux. The diameter and $\sqrt{area}$ of inclusions are respectively reported in the 5$^{th}$ and 6$^{th}$ columns of Table 4-5.

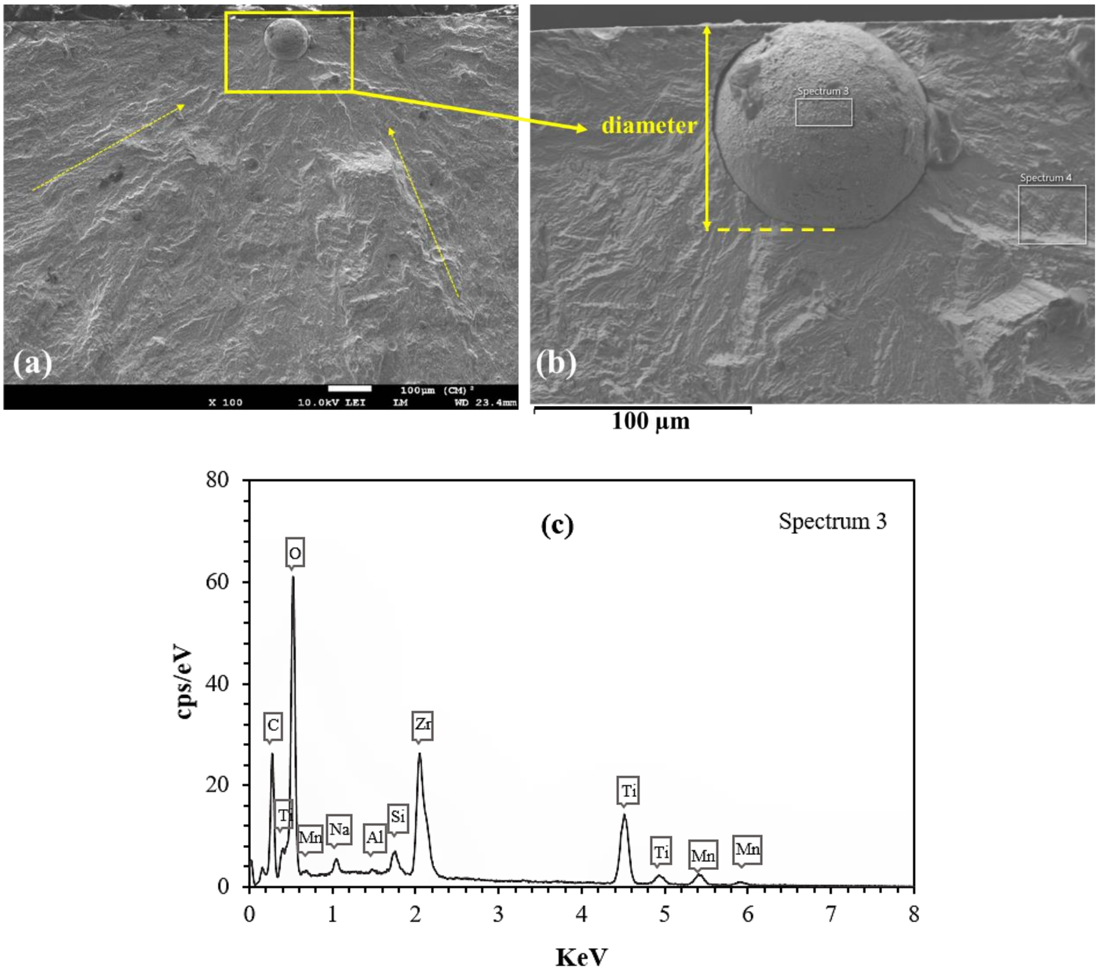


Figure 4-9 (a-b) Fracture surface of specimen N0-2 and (c) EDS results for chemical composition of the inclusion.

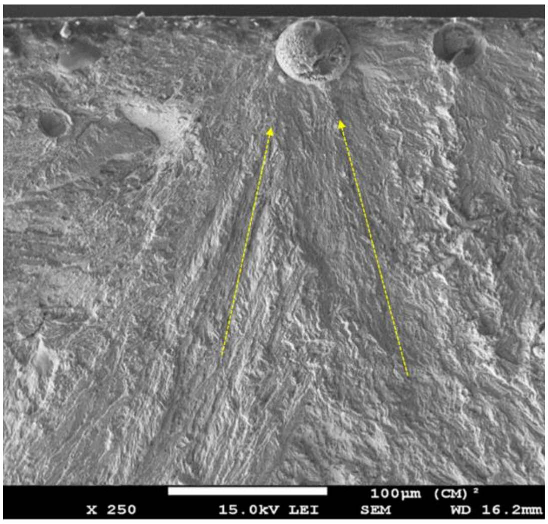


Figure 4- 10 Sub-surface oxide inclusion at the crack initiation site of specimen N0-1.

The type and location of oxide inclusion for both smooth specimens are similar and only the size of discontinuity is different. As reported in Table 4-5, the $\sigma_a$ for N0-1 and N0-2 with inclusion diameters of 39 and 100 µm are 260 and 223 MPa, respectively. For these two specimens, the larger inclusion resulted in a lower fatigue strength as predicted by Murakami [54].

## 4.5.2 Notched specimens

### 4.5.2.1 Fatigue damage without notch effect

Among the 6 specimens with a notch depth of 0.2 mm, four failed outside the notch area. These specimens (N0.2- 1, 2, 3 and 4) had crack initiation from a sub-surface oxide inclusion (similar to smooth specimens N0-1 and N0-2), a porosity or a Mo-rich discontinuity. Figure 4-11 shows a fracture surface where a sub-surface porosity with an average diameter of 70 µm initiated the crack. This porosity could be a gas pore or a void caused by the removal of an oxide during the cleaning operation. According to the EDS results, there was no traces of inclusion inside of this void. Specimen N0.2-1 failed at $\sigma_a$= 239 MPa from a molybdenum rich discontinuity with a size of 203 µm.

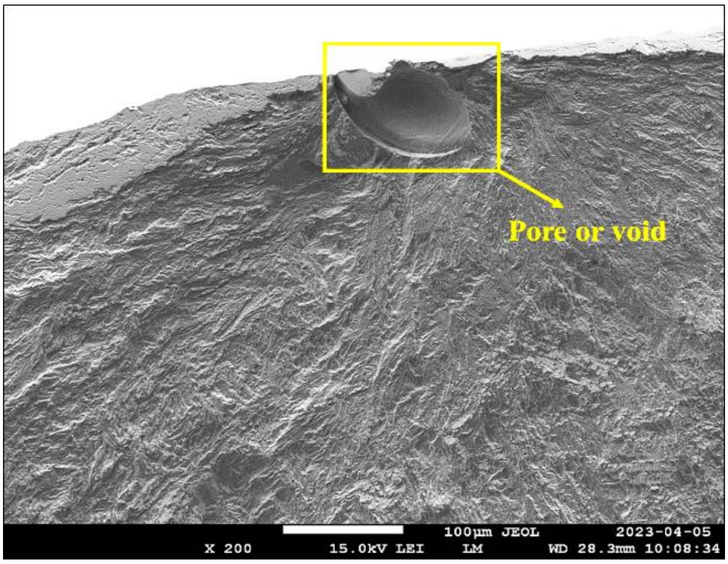


Figure 4-11 Fracture surface of a specimen N0.2-3 showing crack initiation from a pore far from the notch.

As shown in Figure 4-12, a feature commonly referred to as fish-eye was observed around the crack initiation site. The bright rough surface of the inclusion suggests that it is brittle like and it may have cracked during the initiation of the fatigue damage. The EDS results reveal that this discontinuity is reach in molybdenum.

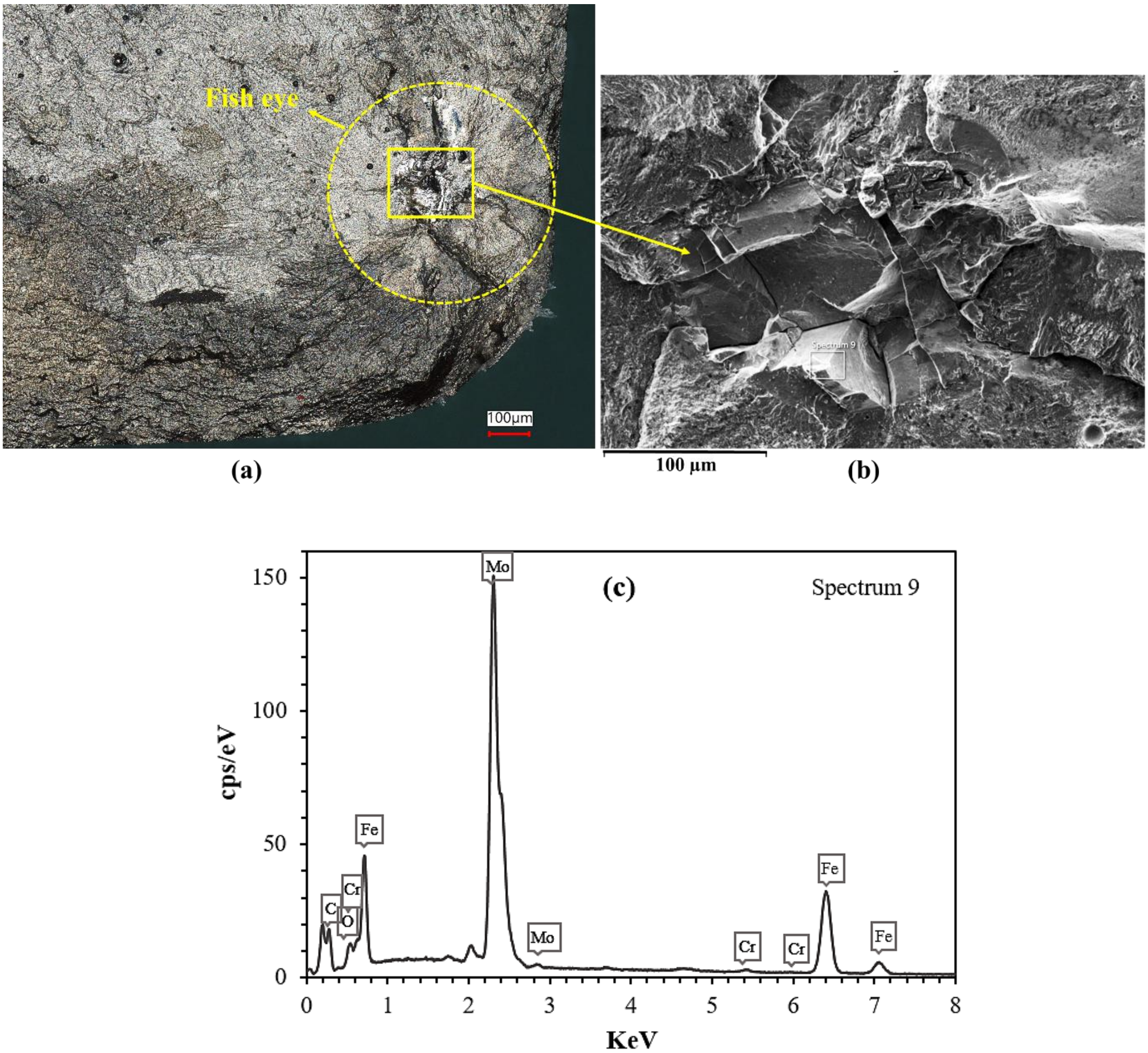


Figure 4-12 (a,b) Fish-eye on the fracture surface of specimen N0.2-1 and (c) its EDS results.

The largest natural discontinuity was found on the fracture surface of specimen N0.2- 4, as shown in Figure 4-13. It is a sub-surface discontinuity with an irregular geometry and a maximum diameter of 312 µm. It triggered the crack initiation and reduced the fatigue strength to a minimum value of 134 MPa. The EDS results revealed that it is rich in molybdenum with very small traces of oxygen and titanium. Amrei et al. [5] confirmed the presence of Mo-rich inclusions in the welded 410NiMo material and suggested that it is likely a particle that was not fully dissolved from the filler material.

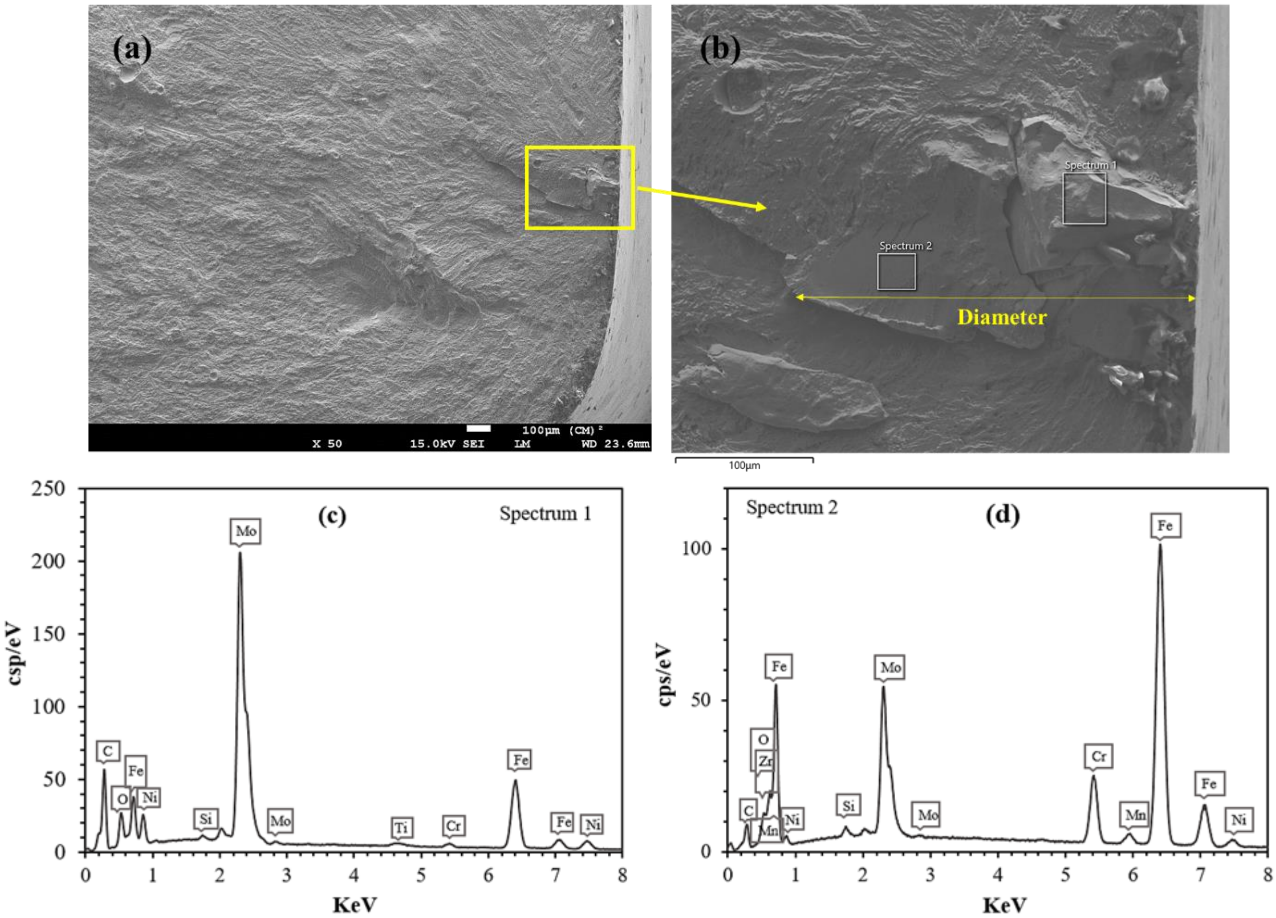


Figure 4-13 (a,b) SEM observation and (c,d) EDS results of the discontinuity on the fracture surface of N0.2-4.

### 4.5.2.2 Fatigue damage with notch effect

Investigation of the fracture surface of samples influenced by the local stress of the notches revealed that cracks could initiate from discontinuity or microstructure. For notch 0.2 mm, two specimens N0.2-5 and N0.2-6 had failure from oxide inclusions (composed of O, Zr, Si, Ti) close to the notch root (see Figure 4-14). The sizes of the oxide inclusions are 12 and 18 µm which is small compared to the previous ones.

By increasing the notch dimensions, some specimens had crack initiation from the microstructure with no visible discontinuity in the fatigue damage area. For instance, the fracture surface of a specimen with notch 0.5 mm is shown in Figure 4-15. No natural discontinuities are observed at the convergence of the ridge lines. Nevertheless, the micro drilling process left tool marks on the surface of the notches and contributed to crack initiation.

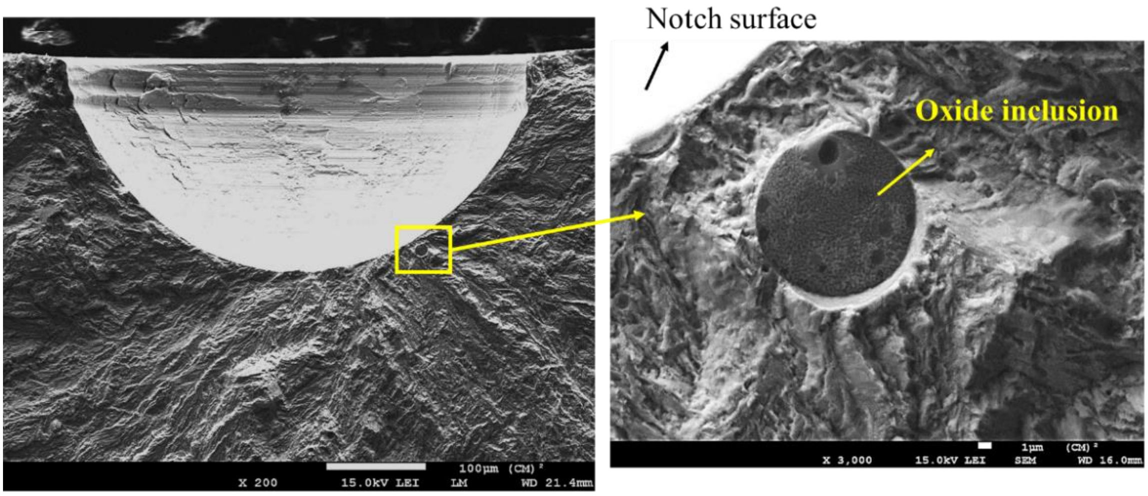


**(a)** **(b)**

Figure 4-14 Fracture surface of specimen with notch 0.2 mm with magnification of (a) 200 X and (b) 3000 X showing potential crack initiation site from oxide inclusion around the notch.

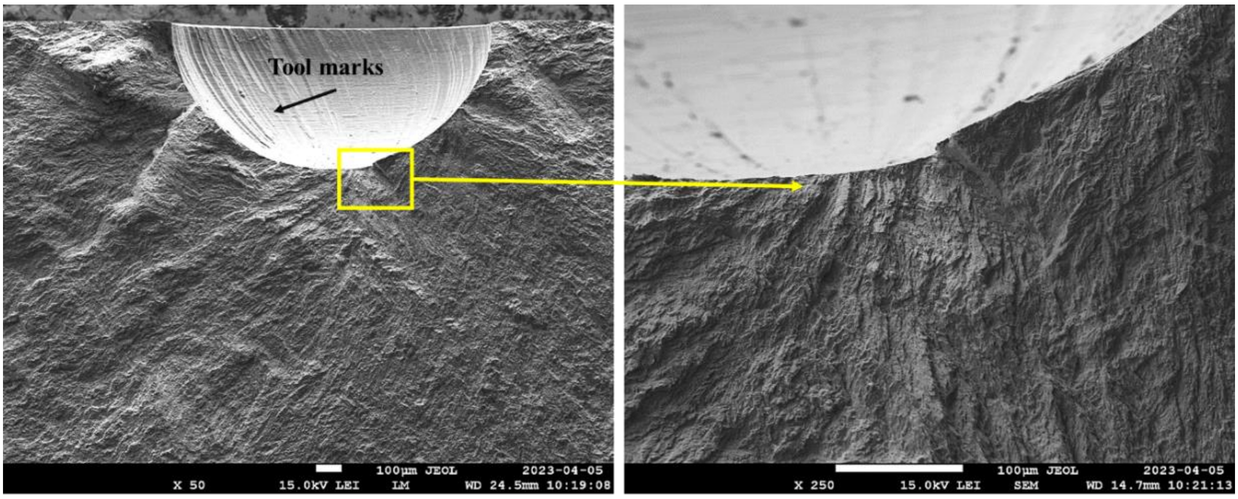


**(a)** **(b)**

Figure 4-15 (a) SEM observations of the fracture surface of specimen with notch radius of 0.5 mm with magnification of 50X and (b) larger magnification at 250X.

## 4.6 Design tool to estimate the fatigue strength of notched specimens

In order to investigate the influence of discontinuity on the fatigue strength, the nominal fatigue strength ($\sigma_a$) of the material as a function of discontinuity size are plotted on a log-log scale, as shown in Figure 4-16. The fatigue results of smooth and NNE specimens are shown by circle points while the fatigue strengths of specimens with notch effect are shown by triangles. Also, the outlier data from NNE specimen is shown by diamond which is ignored for the curve fitting.

On the fracture surface of this specimen (see Figure 4-13), there was a discontinuity with different geometry and size as compare to the natural discontinuities found on the fracture surface of other specimens. Also, despite having a size close to the artificial notches with depth of 0.2 mm, its irregular geometry with brittle-like structure led to a lower fatigue strength compared to the notched specimens. It seems that this discontinuity has a singularity exponent smaller than 0.5 and larger than FEA results for notches (0.16 and 022).

The Kitagawa-Takahashi diagram estimated using the $\Delta K_{th}$ equal to 5.16 MPa$\sqrt{m}$ from the literature and $\sigma_0$= 260 MPa from the experimental fatigue test of smooth specimen (260 MPa is the maximum available fatigue strength for this material) is superimposed to the results. In this figure, it can be seen that the fatigue strength of the specimens with no notch effect (circle points) are within the average range of 245 ± 14 MPa. For the specimens with notch effect, the fatigue strength is reduced with an increase of notch size. However, the decreasing trend (estimated by the dotted line) does not follow the LEFM theory. The difference between the average of the results and the LEFM prediction increases with an increasing defect size. This deviation clearly shows that the artificial defects of this research do not behave like long cracks.

The solid line fitted in Figure 4-17, identical to the dotted line in Figure 4-16, indicates that the singularity exponent of notches equals to 0.18. This value is in good agreement with predicted values found by finite element simulation (0.16 and 0.2 in Z and X direction, respectively). The variation of the AL diagram for $\alpha$ values of 0.16 and 0.2 is schematically shown in Figure 4-17 by blue and red dotted lines, respectively.

The design tool presented in graph of Figure 4-17 was completed by adding a line that represents the blunt notch region where the fatigue strength is expected to be $\frac{\sigma_{a,0}}{k_t}$. In this case, the $\sigma_{a,0}$ value of 260 MPa was used even though all failures initiated from a discontinuity and defect less fatigue resistance is probably above 260 MPa. Also, the $k_t$ value of 2 was calculated from FEA in section 4.3. The transition points of $a_{0,n}$ and $a_n$* were obtained by the intersection of the lines. The $a_{0,n}$ was equal to 0.1 mm representing the smallest size of discontinuity causing a decrease in the fatigue strength. The point $a_n$* is equal to 4.7 mm that is the transition point from the zone governed by stress field ($a < a_n$*) to the peak stress zone ($a > a_n$*). For the notch sizes of $a_{0,n} < a < a_n$*, the notch stress field controls the fatigue strength while if $a > a_n$*, the fatigue strength is dependent on the $k_t$ or the peak stress. Also, the $\Delta K_{th,n}$ is equal to 178 MPa.m$^{0.18}$ for the hemispherical notches and it is calculated by the equation of fitted line for experimental results and Eq. (2-15).

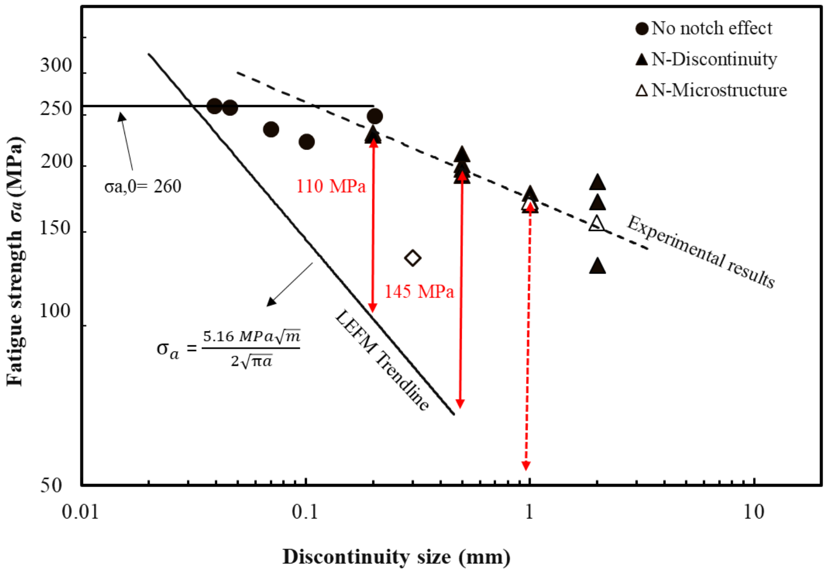


Figure 4-16 Comparison of the K-T diagram with the experimental fatigue results at $R$=0.1, $\zeta$=1 and $N$= 2*10$^{6}$ cycles for welded 410NiMo material.

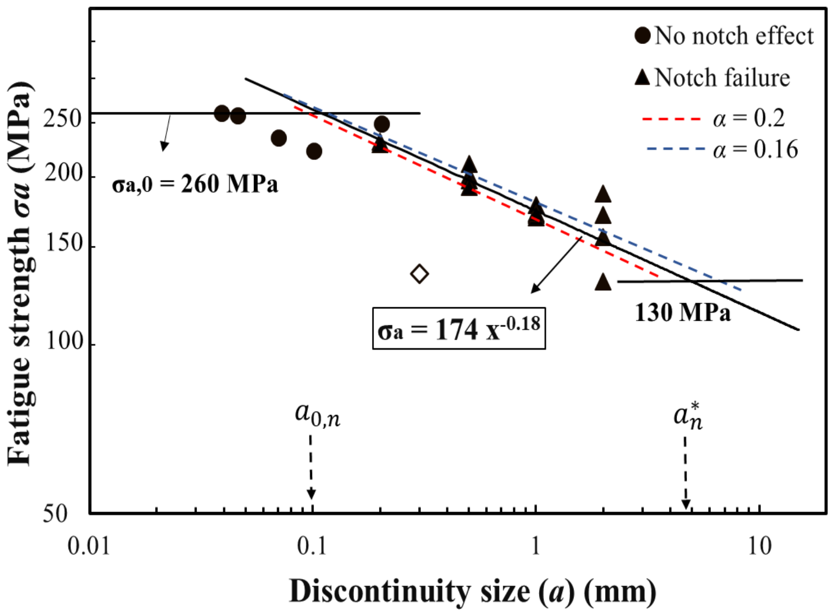


Figure 4-17 Atzori-Lazzarin diagram of the 410NiMo material with $\zeta$= 1, $N$= 2*10$^{6}$ cycles and $R$= 0.1.

## 4.7 Applicability of TCD

The developed A-L diagram of the 410NiMo was obtained using results from experimental fatigue tests. However, to ascertain the reliability of the A-L diagram, it is necessary to check for consistency with fatigue strength prediction of theoretical notch approaches like the TCD (PM and LM) method. Therefore, the TCD plots for the 410NiMo were developed using the curves of stress distribution around the notch (see Figure 4-7), $a_{0,n}$ and the maximum experimental fatigue strength of 260 MPa. An $a_{0,n}$ value of 0.1 mm obtained from Figure 4-17 was used to compute the critical distances of $\frac{a_{0,n}}{2}$ and $2a_{0,n}$ for PM and LM, respectively. Figure 4-18 illustrates the comparison between the average fatigue strength of notched specimens from experiments and the fatigue strength calculated by PM and LM.

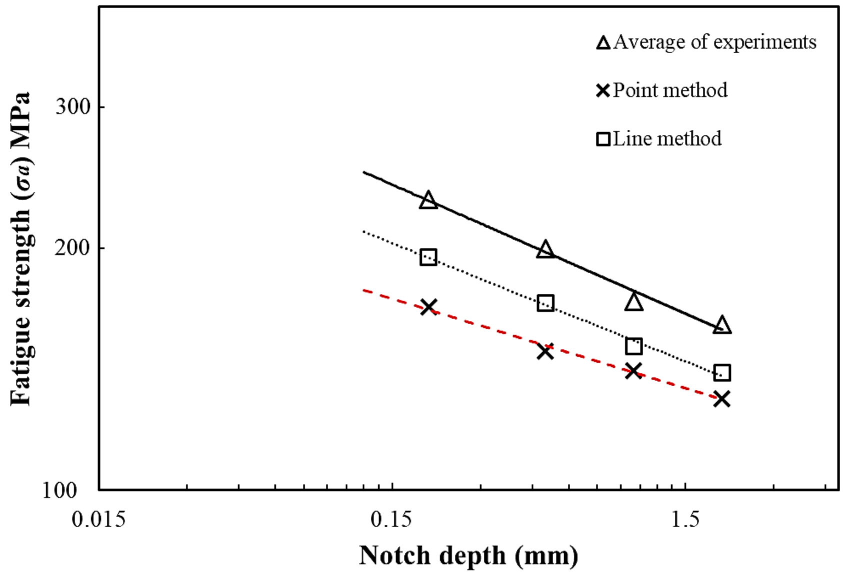


Figure 4-18 Comparison of the fatigue strength of experiments with the predicted values by TCD method using the fatigue limit of 260 MPa.

As shown in Figure 4-18, the TCD method (PM and LM) and experimental results displayed similar slopes which suggests an agreement in the notch singularity. However, the fatigue strength predictions of the TCD method are observed to be different from the experimental data with a rather conservative feature. This difference can be attributed to the input value of 260 MPa used as the real fatigue limit in the analysis to develop the TCD results. However, the real fatigue limit of material is higher than 260 MPa because there was an oxide inclusion at crack initiation site of this fatigue specimen.

Since determination of $\sigma_0$ is difficult for welded 410NiMo material, we can roughly estimate $\sigma_0$ by iterations. The author believes that the $\sigma_0$ for this material is in the range of 300 to 310 MPa. Applying the fatigue limit in this range results in smaller difference between the TCD predictions and experimental data points. Although TCD method is highly dependent on the fatigue limit of material, the A-L diagram for large notches ($a > a_0$) does not rely on the fatigue limit value. For instance, if the actual fatigue limit of material is above 260 MPa, the fitting curve in A-L diagram does not shift to upper stress levels.

Table 4-6 provides a concise overview of the parameters, techniques and required tests for fatigue strength determination in the presence of notches employing the A-L diagram and the TCD method. Calibrating an A-L diagram necessitates various parameters like $\Delta K_{th,n}$, $\sigma_0$ and $k_t$, requiring fatigue tests on both notched and smooth specimens, as well as FEA. Similarly, the TCD method also relies on the fatigue tests, but in this case, the local stress at critical distance from the notch ($\sigma_d$) is determined by FEA. As determining the $\Delta K_{th,n}$ by experiments is challenging, two alternative approaches have been suggested for determining the value of critical distance. In one method, Santus et al.[55] introduced an inverse search method specifically for the sharp V-notched specimen, utilizing point and line-based methods. In this method, the inverse procedure is formulated using complete analytical functions, with the fatigue stress concentration factor as an input instead of $\Delta K_{th}$. The other method, employed by Karakas et al. [56], involves employing a trial-and-error approach, where an iterative process is used to identify the appropriate critical distance.

Table 4- 6 Comparison of the A-L diagram and TCD method (bold parameters are obtained by the stress analysis).

| | **A-L diagram** | **TCD** |
|---|---|---|
| Needed parameters | $\boldsymbol{k_t}, \boldsymbol{\alpha}, \Delta K_{th,n}, \sigma_0$ | $\boldsymbol{\sigma_d}, \Delta K_{th,n}, \sigma_0$ |
| Stress analysis tools | **FEA** (notch stress distribution) | |
| Experimental tests | Fatigue test on notched and smooth specimen | |

The research work has established that the stress singularity associated with discontinuities is influenced by the geometry (shape). Common welding discontinuities like blow holes which are similar to blunt notches will most likely adopt a notch like behavior instead of a crack. Thus, notch approaches are more suitable in design against fatigue for these discontinuities. According to the experimental results, a size limit of 2 mm was noted to be the criteria for blunt notches. Furthermore, the $\Delta K_{th,n}$ for the notch obtained can be used instead of the classical $\Delta K_{th}$ obtained by LEFM in life computation of turbines. This will facilitate optimizing life prediction of turbine systems since current predictions based on crack are over conservative.

In practical case studies, after detecting discontinuities through NDT, when FEA results an $\alpha$ value close to 0.5, the K-T diagram can be employed. However, for blunter discontinuities characterized by smaller $\alpha$ values, calibration of the A-L diagram becomes necessary.

# CHAPTER 5 CONCLUSION AND RECOMMENDATIONS

The main objectives of this project were successfully achieved in three steps. To fulfill the first objective, the finite element simulation was applied to predict the transition conditions from LEFM to the notch theory for 410NiMo weld. Accordingly, the stress concentration factor was determined equal to 2. Also, the singularity exponent in Z and X direction was equal to 0.16 and 0.2, respectively. Using the literature data and FEA results, the transition points of $a_0$ and $a*$ were equal to 0.035 and 0.14 mm for $\alpha$= 0.5, respectively. According to the predicted transition points, the notch dimensions of 0.2, 0.5, 1 and 2 mm were chosen for the experimental fatigue test on notched specimens.

Regarding the second objective, the experimental fatigue tests were performed to validate the predictions in the first objective. In this step, fatigue strength of smooth and notched specimens was determined at $R$= 0.1, $N$= $2*10^6$ cycles and $\zeta$= 1, following the step method testing procedure. Finally, in order to improve the K-T design too by incorporating the notch approach, the A-L diagram and TCD method were used to evaluate the influence of notch-like discontinuities on the fatigue strength.

Completion of the above-mentioned objectives resulted in the following key conclusions:

- In the presence of hemispherical notches, the fatigue strength obtained for notches with a $k_t$ of 2 and $\zeta$ of one with size ranges of 0.2, 0.5, 1 and 2 mm was different from those predicted by the LEFM approach. The minimum difference in the fatigue strength is 110 MPa as the notch size increases from 0.2 to 2 mm.
- The application of the A-L approach, employing the notch stress field, resulted in a singularity exponent of 0.18, which was in good agreement with the predictions derived from the finite element simulations.
- For the hemispherical notches ($\alpha$= 0.18), the parameters $a_{0,n}$ , $a_n*$ and $\Delta K_{th,n}$ are 0.1 mm, 4.7 mm and 178 MPa.m$^{0.18}$, respectively. However, for crack-like notches ($\alpha$= 0.5), these parameters are 0.035 mm, 0.14 mm and 5.16 MPa.m$^{0.5}$, respectively. Hence, crack like notches have a more severe effect on fatigue strength than the hemispherical notches.
- Notches (0.2 mm) in the size ranges of natural discontinuities (46 – 312 µm), are in competition for fatigue crack initiation origin.

Based on the above mentioned results, there are limitations of this research work as follows:

- In the presence of blunt discontinuities in turbine systems, the stress intensity changes and $\Delta K_{th,n}$ should be used instead of the classic $\Delta K_{th}$ from LEFM. Thus, for an optimized fatigue life prediction, the notch approach could be preferable option than the commonly used LEFM. However, the A-L diagram calibrated in this research work is applicable to discontinuities with specific singularity ranging between 0.16 and 0.22 and $k_t$ of 2.0. Its application to other geometries necessitates additional FEA and experimental calibration.

- The state of stress in real cases during service could be different from the laboratory fatigue tests in this research.
- The dimension of fatigue specimens in the laboratory is smaller than the size of turbine runners under cyclic loading.

Accordingly, the following recommendations are put forth to guide and encourage the future research plans:

- Since the acuity of welding discontinuities varies and the A-L diagram is for a unique $k_t$, covering a range of $k_t$ values needs to be developed.
- During the welding process, it's important to be careful to minimize the number and dimensions of welding discontinuities, as bigger ones can act like crack initiation sites that affect the fatigue strength. This could be done by investigating the effect of a welding parameters on the quality of the final part.
- Considering that the turbine runners operate at higher R ratios greater than 0.1 and that turbine runners can endure more than $10^7$ cycles, the applicability of the tool to other loading conditions has to be validated.
- Given that corrosion is an important factor causing failure of turbines, it would be beneficial to assess the impact of notches in the presence of corrosive environment.

# REFERENCES

[1] A. D. Yao, "Analyse statistique des défauts trouvés dans les joints soudés multicouches utilisés dans la fabrication de turbines hydroélectriques," M.S. thesis, Dept. Mech. Eng., École de technologie supérieure, Montreal, Canada, 2021. [online]. Available: https://espace.etsmtl.ca/id/eprint/2959.

[2] R. Ghafoori Ahangar, "Fatigue behavior of welded joints with partial penetration," Ph. D. dissertation, Dept. Mech. Eng., École Polytechnique de Montréal, Montreal, Canada, 2018.

[3] *Standard specification for chromium and chromium-nickel stainless steel plate, sheet, and strip for pressure vessels and for general applications*," ASTM A240, 2022. [online]. Available: 10.1520/A0240_A0240M-22A.

[4] H. Zheng, X. Ye, J. Li, L. Jiang, Z. Liu, G. Wang, B. Wang, "Effect of carbon content on microstructure and mechanical properties of hot-rolled low carbon 12Cr–Ni stainless steel," *Procedia Materials Science*, vol. 527, pp. 7407-7412, 2010. [online]. Available: https://doi.org/10.1016/j.mspro.2015.04.167.

[5] M. M. Amrei, H. Monajati, D. Thibault, Y. Verreman, L. Germain and P. Bocher, "Microstructure characterization and hardness distribution of 13Cr4Ni multipass weld metal,"*Materials Characterization*, vol. 111, pp. 128-136, 2016. [online]. Available: https://doi.org/10.1016/j.matchar.2015.11.022.

[6] H. Habibzadeh Boukani, M. Viens, S.-A. Tahan and M. Gagnon, "Case study on the integrity and nondestructive inspection of flux-cored arc welded joints of Francis turbine runners," *The International Journal of Advanced Manufacturing Technology*, vol. 98, pp. 2201-2211, 2018. [online]. Available: https://doi.org/10.1007/s00170-018-2139-y.

[7] R. Ghafoori-Ahangar and Y. Verreman, "Fatigue behavior of load-carrying cruciform joints with partial penetration fillet welds under three-point bending," *Engineering Fracture Mechanics*, vol. 215, pp. 211-223, 2019. [online]. Available: https://doi.org/10.1016/j.engfracmech.2019.05.015.

[8] M. Gagnon, A. Tahan, P. Bocher and D. Thibault, "On the fatigue reliability of hydroelectric Francis runners," *Procedia Engineering*, vol. 66, pp. 565-574, 2013. [onilne]. Available: https://doi.org/10.1016/j.proeng.2013.12.108.

[9] D. Thibault, M. Gagnon, S. Godin, "The effect of materials properties on the reliability of hydraulic turbine runners," *International Journal of Fluid Machinery and Systems*, vol. 8, pp. 254-263, 2015. [online]. Available: https://doi.org/10.5293/IJFMS.2015.8.4.254.

[10] H. Kitagawa, S. Miyashita, C. Suh and S. Takahashi, "Quantitative analysis of fatigue process microcracks and slip lines under cyclic strains," in: *Fatigue mechanisms*, J.T. Fong, , pp. 420-449, ASTM International, 1979.

[11] D. Taylor, "Geometrical effects in fatigue: a unifying theoretical model," *International Journal of Fatigue*, vol. 21, pp. 413-420, 1999. [online], Available: https://doi.org/10.1016/S0142-1123(99)00007-9.

[12] R. E. Peterson, “Notch sensitivity,” in: *Metal Fatigue*, G. Sines and J. L. Waisman, McGraw-Hill, New York, pp. 293-306, 1959.

[13] H. Neuber, “Kerbspannungslehre. Translation: Theory of notch stresses,” *US Office of Technical Services, Washington DC*, 1958.

[14] B. Atzori and P. Lazzarin, “Notch sensitivity and defect sensitivity under fatigue loading: two sides of the same medal,” *International Journal of Fracture*, vol. 107, pp. 1-8, 2001. [online]. Available: https://doi.org/10.1023/A:1007686727207.

[15] G. C. Silva, J. A. De Castro, R. Filho, L. Caldeira, “Comparing two different arc welding processes through the welding energy: a selection analysis based on quality and energy consumption,” *Journal of the Brazilian Society of Mechanical Sciences and Engineering*, vol. 41, pp. 1-12, 2019. [online]. Available: https://doi.org/10.1007/s40430-019-1804-x.

[16] *Specification for low-alloy steel electrodes and rods for gas shielded arc welding*, ASTM A5.22, 2020.

[17] K. C. Vilela, C. Vaz, “Influence of temperature and time of the double-stage tempering heat treatment on the microstructure and properties of the weld metal 13%Cr- 4%Ni and 0.4% Mo,” *Soldagem & Inspeção*, vol. 25, 2020. [online]. Available: https://doi.org/10.1590/0104-9224/SI25.20.

[18] F. Foroozmehr and P. Bocher, “On the ductile rupture of 13% Cr-4% Ni martensitic stainless steels,” *International Journal of Fracture*, vol. 224, pp. 67-82, 2020. [online]. Available: https://doi.org/10.1007/s10704-020-00446-2.

[19] S. Godin, “Effet d'un enrichissement en nickel sur la stabilité mécanique de l'austénite de réversion lorsque soumise à de la fatigue oligocyclique,” M.S. thesis, Dept. Mech. Eng., École de technologie supérieure, Montreal, Canada, 2014.

[20] Y. Song, X. Li, L. Rong, Y. Li, “The influence of tempering temperature on the reversed austenite formation and tensile properties in Fe– 13%Cr– 4%Ni– Mo low carbon martensite stainless steels,” *Materials Science and Engineering: A*, vol. 528, pp. 4075-4079, 2011. [online]. Available: https://doi.org/10.1016/j.msea.2011.01.078.

[21] B. Tenni, “Étude expérimentale de l'effet du contenu inclusionnaire sur les propriétés mécaniques de résilience et de fatigue-propagation au seuil de soudures en acier 410 NiMo,” M.S. thesis, Dept. Mech. Eng., Ecole Polytechnique Montreal, Montreal, Canada, 2018.

[22] B. Tenni, M. Brochu, S. Godin and D. Thibault, “Shielding gas and inclusion content effects on impact toughness and tensile properties of 410NiMo steel welds,” *Weld. J* 100, vol. 100, pp. 52-62, 2021. [online]. Available: https://doi.org/10.29391/2021.100.005.

[23] J.-B. Lévesque, Unpublished data from Hydro-Québec Research Institute (IREQ), 2022.

[24] U. Zerbst, M. Madia, C. Klinger, D. Bettge and Y. Murakami, “Defects as a root cause of fatigue failure of metallic components. I: Basic aspects,” *Engineering Failure Analysis*, vol. 97, pp. 777-792, 2019. [online]. Available: https://doi.org/10.1016/j.engfailanal.2019.01.055.

[25] R. Aigner, S. Pusterhofer, S. Pomberger, M. Leitner, M. Stoschka, “A probabilistic Kitagawa-Takahashi diagram for fatigue strength assessment of cast aluminium alloys,” *Materials Science and Engineering: A,* vol. 745, pp. 326-334, 2019. [online]. Available: https://doi.org/10.1016/j.msea.2018.12.108.

[26] H. Kitagawa, “Applicability of fracture mechanics to very small cracks or the cracks in the early stage,” *Proc. 2nd Int. Conf. on Mechanical Behaviour of Materials*, pp. 627-631, 1976.

[27] *Standard Practice for Conducting Force Controlled Constant Amplitude Axial Fatigue Tests of Metallic Materials*, ASTM E466, 2021.

[28] *Standard Test Method for Measurement of Fatigue Crack Growth Rates,* ASTM E647, 2023.

[29] N. Dowling, *Mechanical Behavior of Material*, 4th edition, Pearson, 2007.

[30] R. Bolingbroke and J. King, “A comparison of long and short fatigue crack growth in a high strength aluminum alloy,” *The behaviour of short fatigue cracks* pp. 101-114, 1986.

[31] M. El Haddad, K. Smith and T. Topper, “Fatigue crack propagation of short cracks,” *Journal of engineering materials and technology,* vol. 101, pp. 42-46, 1979. [online]. Available: https://doi.org/10.1115/1.3443647.

[32] E. Pessard, M. Lavialle, P. Laheurte, P. Didier and M. Brochu, “High-cycle fatigue behavior of a laser powder bed fusion additive manufactured Ti-6Al-4V titanium: Effect of pores and tested volume size,” *International Journal of Fatigue*, vol. 149, p. 106206, 2021. [online]. Available: https://doi.org/10.1016/j.ijfatigue.2021.106206.

[33] Y. Verreman and N. Limodin, “Fatigue notch factor and short crack propagation,” *Engineering Fracture Mechanics*, vol. 75, pp. 1320-1335, 2008. [online]. Available: https://doi.org/10.1016/j.engfracmech.2007.07.005.

[34] F. Ritz, T. Beck, “Influence of mean stress and notches on the very high cycle fatigue behaviour and crack initiation of a low-pressure steam turbine steel,” *Fatigue & Fracture of Engineering Materials & Structures*, vol. 40, pp. 1762-1771, 2017. [online]. Available: https://doi.org/10.1111/ffe.12666.

[35] S. Kovacs, T. Beck, and L. Singheiser, “Influence of mean stresses on fatigue life and damage of a turbine blade steel in the VHCF-regime,” *International Journal of Fatigue*, vol. 49, pp. 90-99, 2013. [online]. Available: https://doi.org/10.1016/j.ijfatigue.2012.12.012.

[36] M. Ciavarella and G. Meneghetti, “On fatigue limit in the presence of notches: classical vs. recent unified formulations,” *International Journal of Fatigue*, vol. 26, pp. 289-298, 2004. [online]. Available: https://doi.org/10.1016/S0142-1123(03)00106-3.

[37] Y. Liu, C. Deng, B. Gong, Y. He, and D. Wang, “Fatigue limit prediction of notched plates using the zero-point effective notch stress method,” *International Journal of Fatigue*, vol. 151, p. 106392, 2021. [online]. Available: https://doi.org/10.1016/j.ijfatigue.2021.106392.

[38] N. Frost, “A relation between the critical alternating propagation stress and crack length for mild steel,” *Proceedings of the Institution of Mechanical Engineers*, vol. 173, pp. 811-836, 1959. [online]. Available: https://doi.org/10.1243/PIME_PROC_1959_173_065_02.

[39] H. Grover, S. Bishop and L. Jackson, “Axial-load fatigue tests on notched sheet specimens of 24S-T3 and 75S-T6 aluminum alloys and of SAE 4130 steel with stress-concentration factors of 2.0 and 4.0,” *National Aeronautics and Space Administration*, 1951.

[40] S. Usami, I. Takahashi, H. Kimoto, T. Machida and H. Miyata, “Fracture and elevated-temperature static-fatigue of ceramics containing small flaws,” *Advanced Materials for Severe Service Applications,* pp. 119-133, 1987. [online]. Available: https://doi.org/10.1007/978-94-009-3445-0_8.

[41] D. Du Quesnay, M. Yu, T. Topper, “An analysis of notch-size effects at the fatigue limit,” *ournal of testing and evaluation,* vol. 16, pp. 375-385, 1988. [online]. Available: 10.1520/JTE11081J.

[42] B. Atzori, P. Lazzarin, G. Meneghetti, “Fracture mechanics and notch sensitivity,” *Fatigue & Fracture of Engineering Materials & Structures* , vol. 26, pp. 257-267, 2003. [online]. Available: https://doi.org/10.1046/j.1460-2695.2003.00633.x.

[43] B. Atzori, P. Lazzarin and G. Meneghetti, “A unifying approach to fatigue design in presence of defects and notches subject to uniaxial loading,” *MATEC Web of Conferences*, p. 09001, 2014. [online]. Available: https://doi.org/10.1051/matecconf/20141209001.

[44] B. Atzori, P. Lazzarin and G. Meneghetti, “A unified treatment of the mode I fatigue limit of components containing notches or defects,” *International journal of fracture*, vol. 133, pp. 61-87, 2005. [online]. Available: https://doi.org/10.1007/s10704-005-2183-0.

[45] *Standard Practice for Microetching Metals and Alloys*, ASTM E407, 2016.

[46] *Standard Test Method for Microindentation Hardness of Materials*, ASTM E384, 2022.

[47] *Standard Test Methods for Tension Testing of Metallic Materials,* ASTM E8, 2022

[48] M. Williams, “Stress singularities resulting from various boundary conditions in angular corners of plates in extension, ” *Journal of Applied Mechanics*, vol. 19, pp. 526-528, 1952. [online]. Available: https://doi.org/10.1115/1.4010536.

[49] A. D'Andrea, Unpublished data from the research work at École de technologie supérieure, 2023.

[50] T. L. Panontin, *Fatigue and fracture mechanics*, ASTM International, vol. 29, 1999.

[51] M. M. Amrei, H. Monajati, D. Thibault, Y. Verreman, P. Bocher, “Effects of various post-weld heat treatments on austenite and carbide formation in a 13Cr4Ni steel multipass weld,” *Metallography, Microstructure, and Analysis,* vol. 5, pp. 50-61, 2016. [online]. Available: https://doi.org/10.1007/s13632-015-0251-z..

[52] F. Foroozmehr, “Ductile fracture of 13% Cr-4% Ni martensitic stainless steels used in hydraulic turbine welded runners,” M.S. thesis, Dept. Mech. Eng., Ecole Polytechnique, Montreal, Canada, 2017.

[53] J. Chaix, “Influence de la température de revenu sur la résistance du CA6NM à la propagation des fissures de fatigue,” M.S. thesis, Dept. Mech. Eng., École Polytechnique de Montréal, Montreal, Canada, 2014.

[54] Y. Murakami, *Metal fatigue: effects of small defects and nonmetallic inclusions*, Academic Press, 2nd edition, 2019.

[55] C. Santus, D. Taylor, and M. Benedetti, “Determination of the fatigue critical distance according to the Line and the Point Methods with rounded V-notched specimen,” *International journal of fatigue*, vol. 106, pp. 208-218, 2018. [online]. Available: https://doi.org/10.1016/j.ijfatigue.2017.10.002.

[56] Ö.Karakaş , G. Zhang and C. M. Sonsino, “Critical distance approach for the fatigue strength assessment of magnesium welded joints in contrast to Neuber's effective stress method, ” *International Journal of Fatigue*, vol. 112, 21-35, (2018). [online]. Available: https://doi.org/10.1016/j.ijfatigue.2018.03.004.

[57] D. H. Najafabadi, “Characterization of the effect of hydrogen embrittlement on the fatigue crack propagation behaviour of aisi 415 martensitic stainless steel,” M.S. thesis, Dept. Mech. Eng., École Polytechnique de Montréal, Montreal, Canada, 2022..

# APPENDIX A TECHNICAL DRAWINGS

The technical drawings of the tensile specimens and fatigue specimens are presented in Figure A-1 and Figure A-2, respectively.

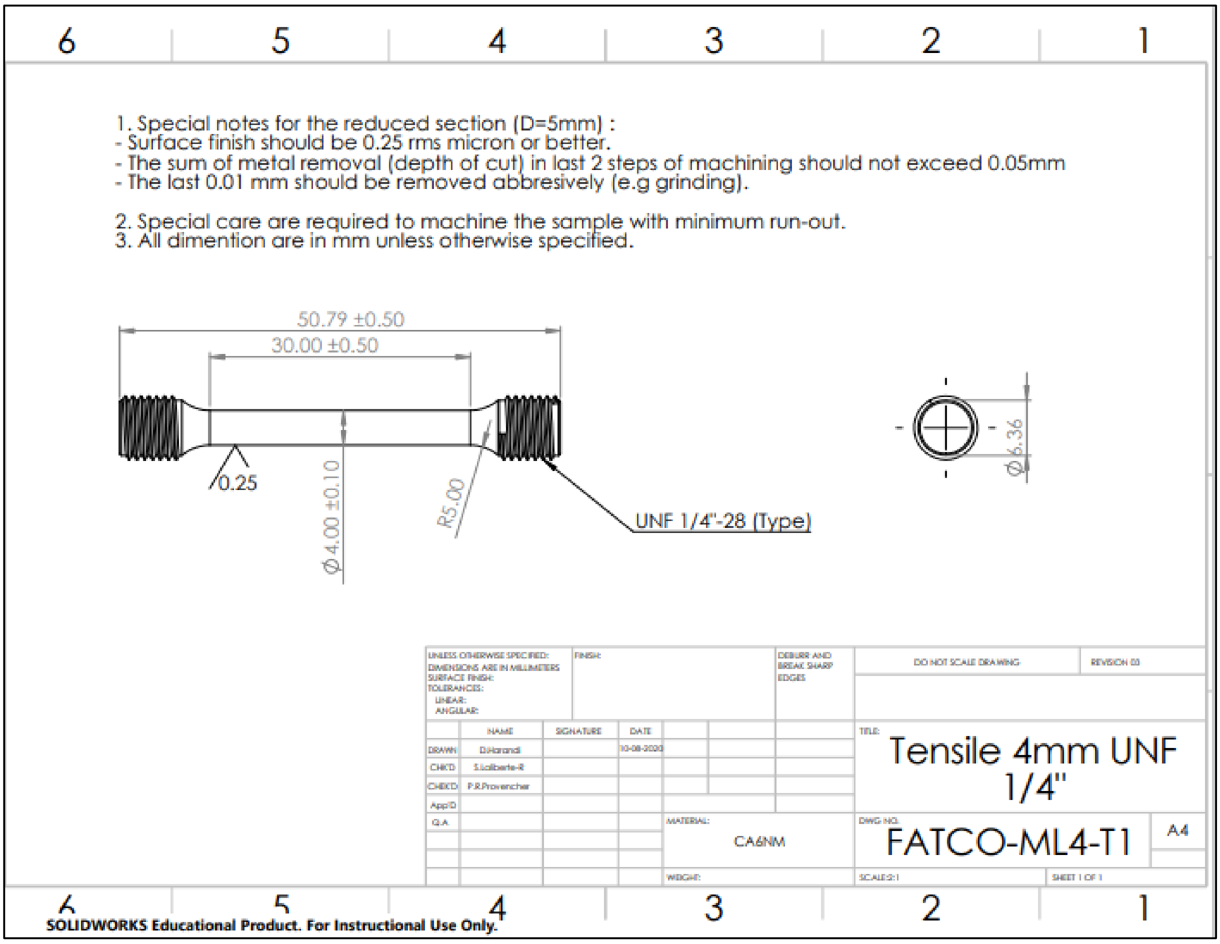


Figure A-1 Manufacturing drawing of tensile specimen [57].

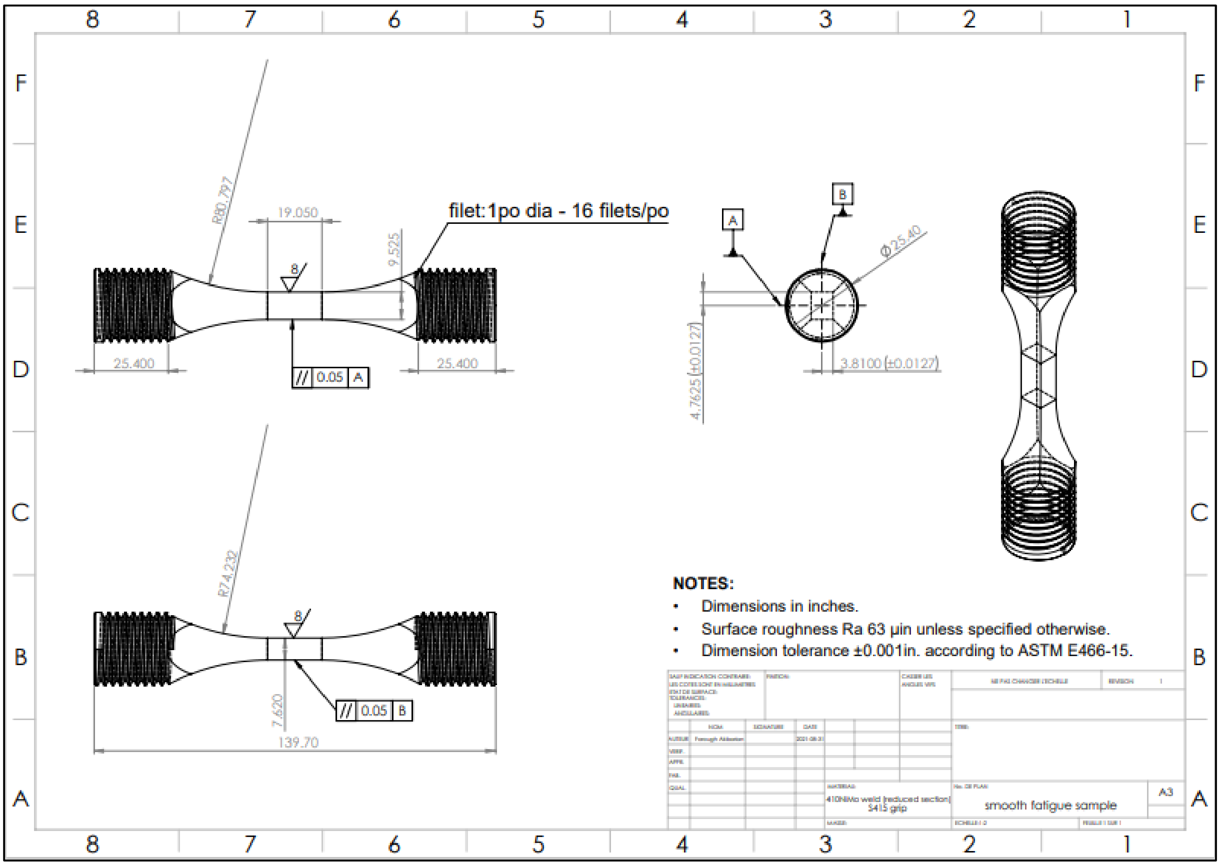


Figure A-2 Manufacturing drawing of fatigue specimen.

# APPENDIX B CALCULATIONS of $\Delta K_{th,n}$ FOR ALUMINUM ALLOY

According to Eq. (2-14):

$$a_{0,n} = \left(\frac{\Delta K_{th,n}}{\sqrt{\pi}.\Delta\sigma_0}\right)^{\frac{1}{\alpha}}$$

For stress ranges different from $\Delta\sigma_0$, the equation changes as below:

$$a_n = \left(\frac{\Delta K_{th,n}}{\sqrt{\pi}.\Delta\sigma}\right)^{\frac{1}{\alpha}}$$

Therefore:

$$\Delta\sigma = \frac{\Delta K_{th,n}}{\sqrt{\pi}} \, . \, a_n^{-\alpha}$$

The equation of fitted line in Figure 2-16 is:

$$\Delta\sigma = 52.2 \, a^{-0.326}$$

And refferning to the general equation, the constant coefficient 52.2 is defined as below:

$$\frac{\Delta K_{th,n}}{\sqrt{\pi}} = 52.2 \quad \text{MPa.(mm)}^{0.326}$$

$$\Delta K_{th,n} = 52.2 * \sqrt{\pi} = 92.5 \quad \text{MPa. (mm)}^{0.326}$$

# APPENDIX C STRESS DISTRIBUTION IN X-AXIS

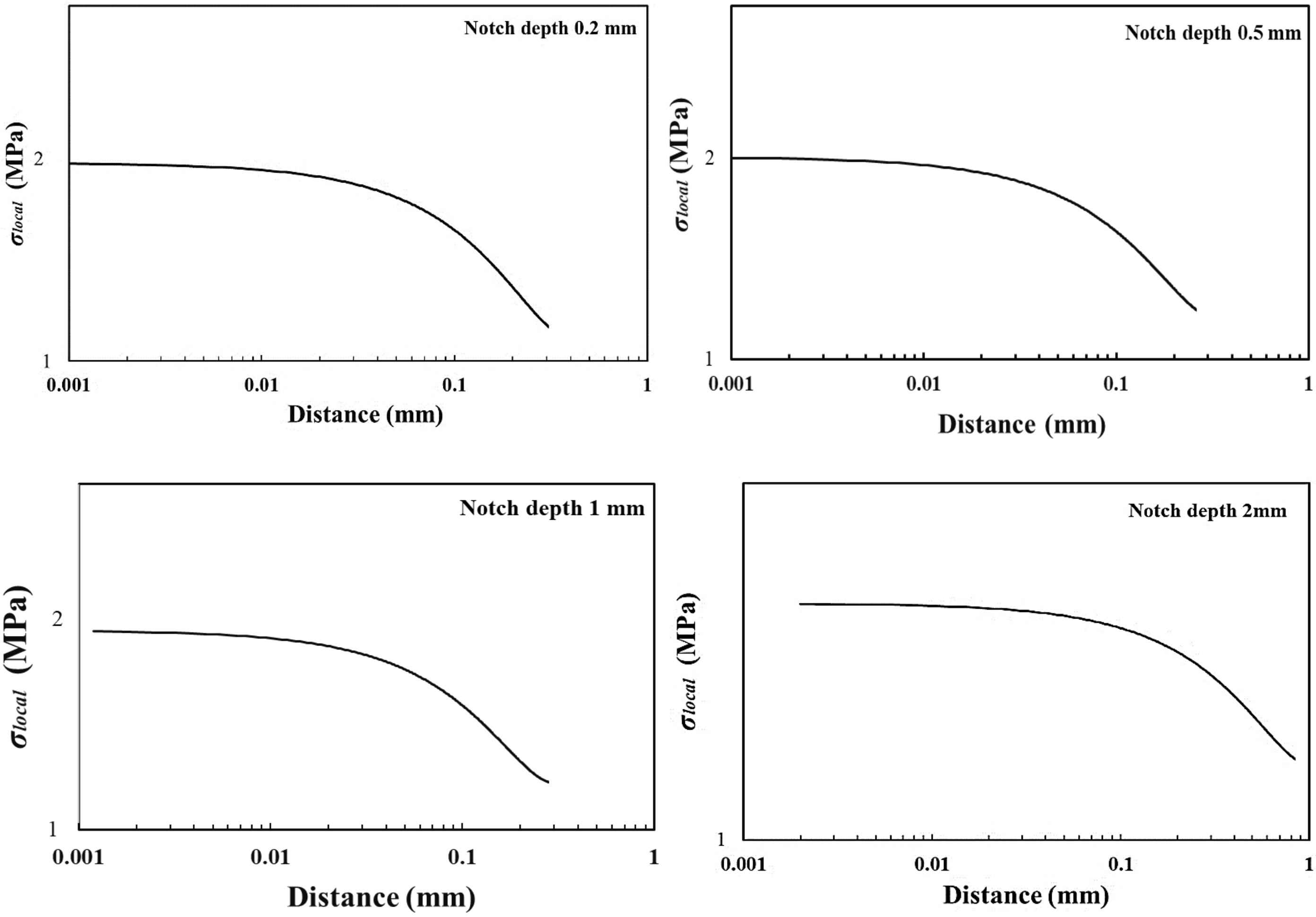


Figure A-3 Stress distribution around notches in X-axis.

# APPENDIX D CALCULATION OF $\Delta K_{th,n}$ FOR NOTCHES WITH ACUITY OF ONE

According to the equation of the fitted line in Figure 4-17:

$\sigma_a = 174\, x^{-0.18}$

According to Eq. (2-15),

$\Delta\sigma_a = 2*174\, x^{-0.18}$

$\frac{\Delta K_{th,n}}{\sqrt{\pi}} = (348)$ MPa.(mm)$^{0.18}$

Or $\frac{\Delta K_{th,n}}{\sqrt{\pi}} = (100.36)$ MPa.(m)$^{0.18}$

Then: $\Delta K_{th,n} = 178$ MPa.(m)$^{0.18}$

When $a_{0,n} = 0.1$ (intersection point of threshold line and the fatigue limit) and $k_t = 2$,

$a_n^{*} = a_{0,n} * (k_t)^{\frac{1}{0.18}} = 4.7$ mm